ACS NANO

www.acsnano.org

ARTICLE

Hyaluronan Nanoparticles Selectively Target Plaque-Associated Macrophages and Improve Plaque Stability in Atherosclerosis

Thijs J. Beldman,[†] Max L. Senders,[†] Amr Alaarg,[‡,§] Carlos Pérez-Medina,[‡] Jun Tang,[‡,¶] Yiming Zhao,[‡] Francois Fay,[‡] Jacqueline Deichmöller,[⊥,∥] Benjamin Born,[⊥] Emilie Desclos,[#] Nicole N. van der Wel,[#] Ron A. Hoebe,[#] Fortune Kohen,[⊥] Elena Kartvelishvily,[□] Michal Neeman,[⊥] Thomas Reiner,[¶,△] Claudia Calcagno,[‡] Zahi A. Fayad,[‡] Menno P. J. de Winther,[†,▽] Esther Lutgens,[†,▽] Willem J. M. Mulder,[†,‡] and Ewelina Kluza*[,†]

[†]Experimental Vascular Biology, Department of Medical Biochemistry, and [#]Cellular Imaging, AMC Core Facility, Academic Medical Center, Amsterdam 1105 AZ, The Netherlands

[‡]Department of Radiology, Mount Sinai School of Medicine, New York, New York 10029, United States

[¶]Department of Radiology, Memorial Sloan Kettering Cancer Center, New York, New York 10065, United States

[§]Department of Biomaterials Science and Technology, MIRA Institute for Biomedical Technology and Technical Medicine, University of Twente, Enschede 7522 NB, The Netherlands

[⊥]Department of Biological Regulation and [□]Department of Chemical Research Support, Weizmann Institute of Science, Rehovot 7610001, Israel

[∥]Physical Chemistry II, Ruhr-Universität Bochum, Bochum 44801, Germany

[△]Department of Radiology, Weill Cornell Medical College, New York, New York 10065, United States

[▽]Institute for Cardiovascular Prevention, Ludwig Maximilians University, Munich 80336, Germany

Supporting Information

ABSTRACT: **Hyaluronan is a biologically active polymer, which can be formulated into nanoparticles. In our study, we aimed to probe atherosclerosis-associated inflammation by using hyaluronan nanoparticles and to determine whether they can ameliorate atherosclerosis. Hyaluronan nanoparticles (HA-NPs) were prepared by reacting amine-functionalized oligomeric hyaluronan (HA) with cholanic ester and labeled with a fluorescent or radioactive label. HA-NPs were characterized *in vitro* by several advanced microscopy methods. The targeting properties and biodistribution of HA-NPs were studied in *apoe*$^{-/-}$ mice, which received either fluorescent or radiolabeled HA-NPs and were examined *ex vivo* by flow cytometry or nuclear techniques. Furthermore, three atherosclerotic rabbits received ^{89}Zr-HA-NPs and were imaged by PET/MRI. The therapeutic effects of HA-NPs were studied in *apoe*$^{-/-}$ mice, which received weekly doses of 50 mg/kg HA-NPs during a 12-week high-fat diet feeding period. Hydrated HA-NPs were *ca.* 90 nm in diameter and displayed very stable morphology under hydrolysis conditions. Flow cytometry revealed a 6- to 40-fold higher uptake of Cy7-HA-NPs by aortic macrophages compared to normal tissue macrophages. Interestingly, both local and systemic HA-NP−immune cell interactions significantly decreased over the disease progression. ^{89}Zr-HA-NPs-induced radioactivity in atherosclerotic aortas was 30% higher than in wild-type controls. PET imaging of rabbits revealed 6-fold higher standardized uptake values compared to the muscle. The plaques of HA-NP-treated mice contained 30% fewer macrophages compared to control and free HA-treated group. In conclusion, we show favorable targeting properties of HA-NPs, which can be exploited for PET imaging of atherosclerosis-associated inflammation. Furthermore, we demonstrate the anti-inflammatory effects of HA-NPs in atherosclerosis.**

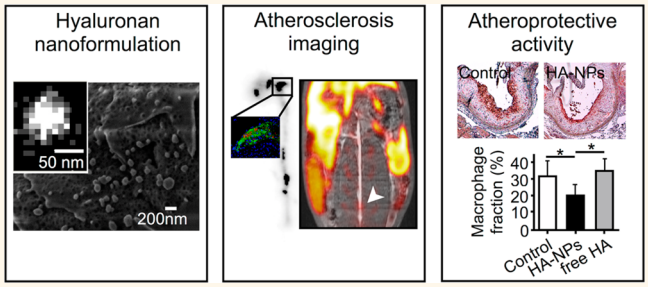

KEYWORDS: *hyaluronan nanoparticles, atherosclerosis, inflammation, PET imaging, anti-inflammatory effects, antiatherogenic therapy*

Received: February 27, 2017
Accepted: May 2, 2017
Published: May 2, 2017

DOI: 10.1021/acsnano.7b01385
ACS Nano 2017, 11, 5785−5799

Hyaluronan (HA) is a linear polymer consisting of *N*-acetylglucosamine and a β-glucuronic acid, which displays distinctive physicochemical and biological properties.[1] As a key component of the extracellular matrix, it effectively lubricates and binds water, and, by interacting with several hyaluronan receptors, hyaluronan regulates cell adhesion, migration, and proliferation.[2] During inflammation, the hyaluronan lining on vascular endothelium mediates immune cell rolling and extravasation, and at the site of inflammation the hyaluronic-rich microenvironment stimulates the tissue penetration by and division of immune cells.[3] In oncology, hyaluronan−CD44 receptor interactions have been proposed as key players in tumor progression and metastasis.[4−7] Notably, the biological activity of hyaluronan depends strongly on its degree of polymerization. Low-molecular-weight hyaluronan oligomers have been shown to stimulate inflammation and angiogenesis,[8−12] whereas highly polymerized (multi) megadalton (MDa) hyaluronan acts as a suppressor of these processes.[8−10,13−16]

The aforementioned properties, nonimmunogenicity, and cost-effective production of hyaluronan have propelled its application in biomedicine. At present, hyaluronan's local administration is applied in arthrology, ophthalmology, and esthetic medicine,[17,18] but its systemic application is highly challenging due to rapid blood clearance[19−22] and susceptibility to hydrolysis. In this respect, hyaluronan-based therapeutics might benefit from nanomedicine-based formulation strategies, which have shown their tunability for cellular interactions[23] and profound impact on the pharmacokinetic properties of various biomaterials.[24,25] Although hyaluronan has been deposited on the surface of either lipid or polymeric nanoparticles, studies exploiting the polymeric backbones of hyaluronan for nanoparticle assembly, which can be achieved by chemical modification of hyaluronan carboxyl groups, are scarce.[26−32]

In our study, we exploit hyaluronan suprachemistry to formulate nanoparticles, which we propose for targeting of atherosclerosis-associated inflammation.[33−36] This is motivated by the critical role of hyaluronan−immune cell interactions during the inflammatory processes,[3] which drive the atherosclerosis progression and severe complications.[37,38] The diagnosis and treatment of high-risk patients still remains an unresolved problem.[39,40] Macrophages, the key propagators of atherosclerosis and primary phagocytes in atherosclerotic plaques, express several hyaluronan-binding receptors, including CD44, ICAM-1, LYVE-1, RHAMM, and TLR-4.[41−44] Notably, macrophages are a highly dynamic cell population, the molecular and functional profile of which is strongly influenced by the tissue microenvironment.[45,46] The assessment of these phenotypic alternations may be of important predictive and prognostic value in atherosclerosis.

In view of the rapid hyaluronan degradability, we extensively studied the morphological and chemical stability of nanoparticle (NP)-formulated hyaluronan. To this aim, we employed several advanced microscopy methods, including atomic force microscopy, cryo-scanning electron microscopy, and super-resolution fluorescence microscopy. Flow cytometry allowed us to study the nature of the interactions between nanoparticulate hyaluronan and immune cells and how the atherosclerotic plaque progression affects these interplays. Furthermore, we performed radiolabeling of HA-NPs with ^{89}Zr for quantitative evaluation of plaque targeting efficacy, clearance kinetics, and biodistribution in atherosclerotic *apoe*$^{-/-}$ mice. The translational impact of ^{89}Zr-HA-NPs was investigated by noninvasive imaging of atherosclerotic rabbits using a fully integrated positron emission tomography and magnetic resonance imaging (PET/MRI) system. We also investigated the impact of hyaluronan assembly into nanoparticles on its biological activity, by probing the atheroprotective effects of HA-NPs.

RESULTS AND DISCUSSION

Morphology of Hyaluronan-Based Nanoparticles and the Impact of Hydrolysis. To determine the morphological characteristics of hyaluronan-based nanoparticles (HA-NPs) and their stability under hydrolytic conditions, we applied several advanced microscopy methods (Figure 1A). Atomic force microscopy (AFM) revealed that the air-dried HA-NPs were spherical structures with a mean diameter of 32 ± 0.5 nm (Figure 1A,B, first panel). Interestingly, after hyaluronidase (HYAL) treatment, the nanoparticles were still highly abundant and their size changed only marginally; that is, we observed them to be 26 ± 5.1 nm in diameter. Cryo-scanning electron microscopy (cryo-SEM) of a snap-frozen sample of HA-NPs in buffered saline showed larger nanoparticles of *ca.* 80 nm in diameter (Figure 1A, second panel). In the HYAL-treated samples, the nanoparticles were also readily present. Wet-mode environmental SEM (ESEM) showed larger aggregates of HA-NPs compared to all other methods, which was likely induced by the surface drying (Figure 1A, third panel). Interestingly, hydrolyzed HA-NPs appeared to retain more water, as deduced from their lower image contrast at higher vacuum. Direct stochastic optical reconstruction microscopy (dSTORM) analysis of surface-immobilized Cy5.5-labeled HA-NPs in aqueous conditions revealed the presence of fluorescent nanostructures with a median diameter of 90 nm (Figure 1A,B). HYAL treatment did not affect the nanoparticle size considerably. Notably, however, Cy5.5 blinking events appeared to be more disperse for HYAL-treated nanoparticles. In contrast, dSTORM images of disulfo Cy5-COOH, which was used as a small-molecular-weight control, showed diffusely distributed Cy5 molecules and only a small degree of molecule aggregation (Figure S1, Supporting Information).

The hydrolytic stability of HA-NPs was established by dynamic light scattering (DLS). Interestingly, the mean hydrodynamic diameter increased from 100 nm to 125 nm after HYAL treatment (intensity-based) (Figure S2A, Supporting Information). Under both neutral and hydrolytic conditions, there was a small peak (∼10−20%) of larger aggregates of 600−800 nm. The zeta potential marginally changed from −31.3 ± 2.6 mV to −33.3 ± 2.2 mV, indicative of a stable nanosuspension. In comparison, the hydrolysis of high-molecular-weight HA resulted in a zeta potential drop from −19.0 ± 0.5 mV to −8.5 ± 1.2 mV. A summary of quantitative parameters obtained for HA-NPs and HYAL-treated counterparts by different methods is displayed in Figure S2B.

HA-NPs and their hydrolysis products were further analyzed by size exclusion chromatography (Figure S3, Supporting Information). The median retention time (t_R) of HA-NPs was *ca.* 9 min, which indicates MDa structures. Hydrolyzed HA-NPs displayed a rather small shift toward longer t_R, *i.e*, the median t_R of about 12 min, ∼300 kDa. The size distribution was broader but, to a large extent, overlapping with that of HA-NPs. In the case of free HA, our data indicate its aggregation into large structures, *i.e*, above the exclusion limit of 1.3 MDa. However, HA hydrolysis resulted in the formation of smaller HA products, ranging between 50 kDa and several hundreds of Da. The aforementioned results show therefore different effects of hydrolysis on the NP-formulated HA compared to the linear counterpart.

DOI: 10.1021/acsnano.7b01385
ACS Nano 2017, 11, 5785−5799

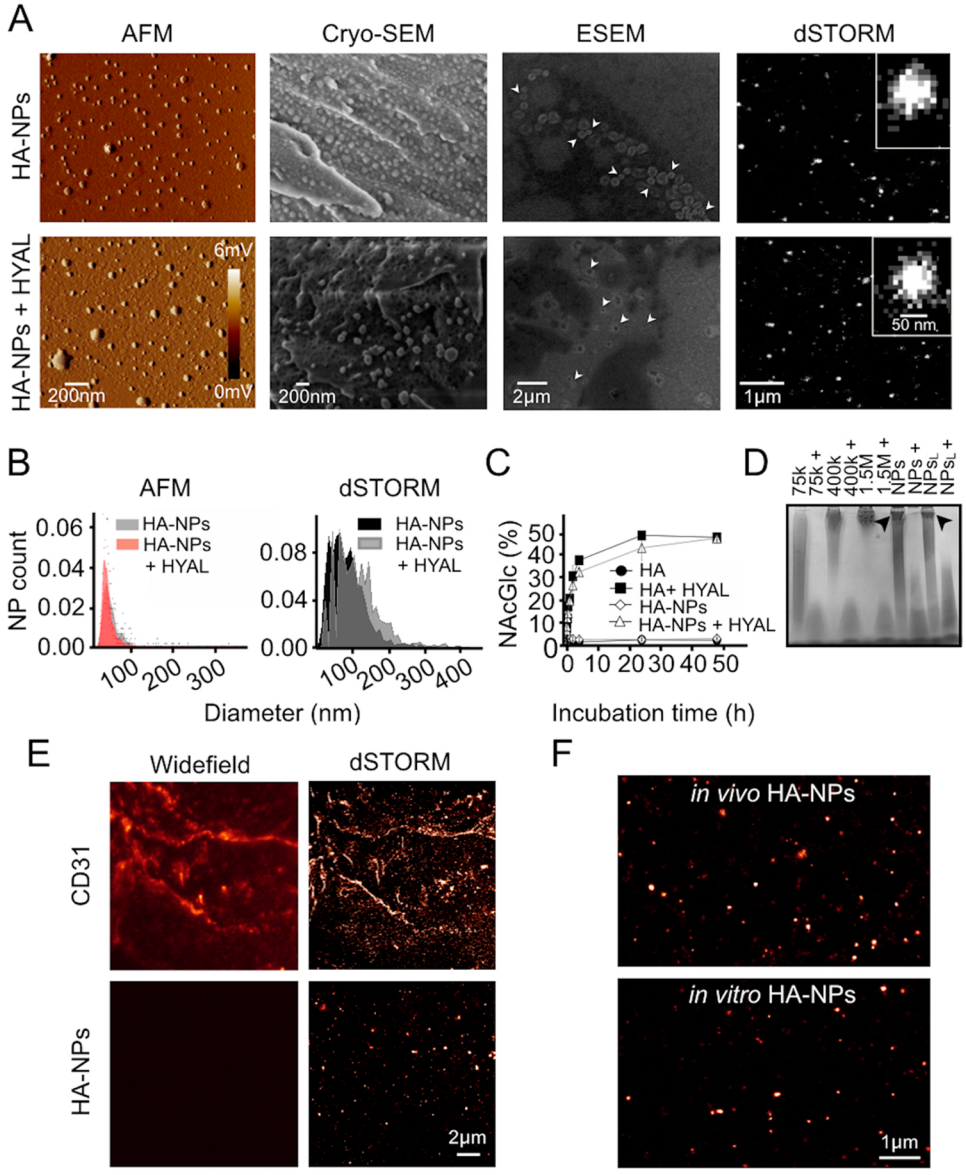

Figure 1. (A) Hyaluronan nanoparticles (HA-NPs) (upper panel) and HA-NPs after hyaluronidase (HYAL) treatment (lower panel) visualized by atomic force microscopy (AFM) (first panel), cryo-scanning electron microscopy (cryo-SEM) (second panel), environmental scanning electron microscopy (ESEM) (third panel), and direct stochastic optical reconstruction microscopy (dSTORM) (fourth panel). The scale bars shown in the lower images refer also to the upper images. White arrowheads in ESEM images indicate the location of nanoparticles. The image insets in the fourth panel show representative dSTORM images of a single nanoparticle at higher magnification. (B) Normalized distribution of nanoparticle diameter obtained from AFM (left panel) and dSTORM (right panel) data. In the left panel, the size distribution of HA-NPs and hydrolyzed HA-NPs (HA-NPs + HYAL) is shown in gray and red, respectively, and, in the right panel, in black and gray, respectively. (C) Amount of terminal *N*-acetylglucosamine (NAcGlc) released from hyaluronan (HA) and HA-NPs during hydrolysis with HYAL, which is expressed as the percentage of total NAcGlc of substrate hyaluronan. (D) Transmitted light image of stained polyacrylamide gel showing the migration spots of different molecular weight hyaluronan, *i.e.*, ~75 kDa (75k), ~400 kDa (400k), and ~1.5 MDa (1.5M), nonlabeled hyaluronan nanoparticles (NPs), fluorescently labeled HA-NPs (NPs_L), and their hydrolysis products. Symbol "+" indicates the hydrolyzed samples. Two black arrowheads point at the poorly migrating high-molecular-weight hyaluronan in HA-NP samples. (E) Wide-field (left panel) and two-color dSTORM (right panel) microscopy images of aortic endothelium of a mouse that received an injection of Cy5.5-HA-NPs 2 h before sacrifice. Endothelial cells were stained with CD31-Alexa Fluor 555. (F) Comparison of HA-NP morphology in a mouse aortic endothelium after the *in vivo* administration of Cy5.5-HA-NPs and on a coverglass after the *in vitro* seeding of Cy5.5-HA-NPs, assessed by dSTORM. Scale bars in lower images refer to those in the upper panel.

At the same time, we observed the intrinsic aggregation of oligomeric HA under the investigated conditions.

Moreover, to determine the morphology of *in vivo*-administered HA-NPs, we applied super-resolution microscopy (dSTORM). In Figure 1E, we show representative wide-field and dSTORM images of aortic endothelium with the engulfed HA-NPs, which could be visualized and spatially resolved exclusively by the dSTORM technique. The observed NP morphology corresponded to that of the *in vitro* visualized counterparts (Figure 1F), indicative of HA-NPs' stability under *in vivo* conditions.

The visualization of HA supramolecular structure in solution is very challenging due to its high hydrophilicity.[47] We demonstrated that HA-NPs can be successfully visualized in the hydrated

DOI: 10.1021/acsnano.7b01385
ACS Nano 2017, 11, 5785−5799

state by cryo- and environmental SEM and indirectly by dSTORM (Figure 1A). The 3- to 4-fold higher NP size in aqueous conditions compared to the AFM-assessed dried form reflects the high water-binding properties of HA-NPs. Importantly, all the applied methods showed the limited impact of hydrolysis on the nanoparticle morphology and size distribution. Intriguingly, the release of terminal *N*-acetylglucosamine, which is a consequence of glycoside bond breakdown by HYAL, was only slightly lower for HA-NPs compared to free HA (Figure 1C). It needs to be stressed that both the HA cross-linking and conjugation of cholanic ester, which occur during NP assembly, do not affect the glycosidic bonds. This is in line with the unaltered HYAL activity. At the same time, the electrophoresis experiment revealed the presence of larger oligomeric products in HYAL-treated HA-NPs (NPs+ and NPs_L+) compared to free HA formulations (75k+ , 400k+, and 1.5M+) (Figure 1D). This implies the presence of stable bonds in HA-NPs, which resisted the HYAL digestion. In the same experiment, the untreated HA-NPs displayed poor gel migration, corresponding to that of high-molecular-weight hyaluronan (≥1.5 MDa), but also contained some oligomeric HA. NPs and NPs+ therefore displayed a different migration profile, which is in contrast to the results by microscopy or DLS. Possibly, the high voltage used for electrophoresis (300 V) was able to dissociate oligomeric components of NPs+, which does not occur under neutral conditions.

From the aforementioned experiments, we can conclude that NP-incorporated HA undergoes hydrolysis, which does not lead to NP disintegration. We believe that the breakdown of glycoside bonds leads to a decreased HA packing in HA-NPs, as suggested by DLS and dSTORM measurements. At the same time, HA cross-linking by enthylenediamine bridges as well as its covalent and amphiphilic interactions[48] with hydrophobic cholanic acid molecules prevented the nanoparticles from disintegrating.

Selectivity of Hyaluronan Nanoparticles toward Pro-inflammatory Macrophage Phenotype. The targeting properties of HA-NPs were studied *in vitro* in bone-marrow-derived macrophages (BMDMs), which were differentiated into several macrophage phenotypes using oxidized low-density lipoprotein (oxLDL), interleukin-4 (IL-4), or lipopolysaccharide (LPS) and interferon-γ (INFγ). The cellular uptake of HA-NPs was measured by flow cytometry, which is displayed in Figure 2A (upper panel). The LPS-stimulated macrophages, which represent the pro-inflammatory macrophage phenotype, displayed the highest uptake of HA-NPs. It was *ca.* 3-fold higher compared to the naive and anti-inflammatory (IL-4) macrophages. Interestingly, oxLDL, which is an important pro-atherogenic factor,[49] significantly decreased the HA-NP uptake efficacy in pro-inflammatory macrophages by approximately 30% (p = 0.0043). Similar experiments were performed for Cy5-labeled free HA and Cy5.5-labeled dextran-NPs (Figure S4A). In contrast to HA-NPs, relative differences between the investigated macrophage phenotypes were much less apparent after incubation with free HA or dextran-NPs. Interestingly, and in line with the HA-NP findings, oxLDL decreased the uptake of HA by 50%. Although oxLDL is a recognized pro-atherogenic factor, its *in vitro* effects on macrophages are unclear, particularly in LPS-stimulated pro-inflammatory macrophages.[50] As oxLDL is a poor inducer of foam cell formation under *in vitro* conditions, the lipid loading of macrophages cannot underlie the observed drop in HA-NP uptake efficacy. Alternatively, oxLDL can act as a competitor for the scavenger receptors CD36 and SR-A, which might lead to a decreased HA-NP uptake.

Phagocytosis is the primary mechanism driving nanoparticle engulfment by macrophages.[51,52] However, we also considered an additive effect of HA-NP interaction with hyaluronan receptors, expressed by macrophages.[41−44] We therefore studied the effects of different stimuli on the expression of hyaluronan receptors in BMDMs and how it relates to HA-NP−receptor interactions and overall HA-NP uptake. Flow cytometry analysis revealed the overexpression of almost all hyaluronan receptors, except for ICAM-1, by IL-4-stimulated (anti-inflammatory) macrophages (Figure S4A, right panel) (Supporting Information). This correlated well with the enhanced cell membrane association of HA-NP at 4 °C, as visualized by confocal microscopy (Figure S4B). Notably, however, this enhanced hyaluronan receptor expression did not lead to more efficient HA-NP engulfment, as shown in Figure 2A. Furthermore, we performed competition experiments with free HA and CD44 antibody. Interestingly, only in the case of LPS-treated (pro-inflammatory) macrophages did the competition with free HA lead to a significant decrease in the HA-NP uptake (Figure S4C). Anti-CD44 antibody had no or a positive impact on HA-NP uptake (Figure S4C). It needs to be stressed that previous studies have shown that hyaluronan and CD44 antibodies can bind to different sites on the CD44 receptor.[53] Furthermore, CD44-mediated hyaluronan binding to macrophages requires activation of the receptor.[54,55] We also cannot exclude the interference of LPS contamination of anti-CD44 antibody in the latter experiment.

Hyaluronan Nanoparticles Target Plaque-Associated Macrophages in Atherosclerotic Mice. The *in vivo* targeting efficacy and selectivity of HA-NPs were studied in *apoe*$^{-/-}$ mice, in which either early or advanced atherosclerosis was induced by a six- (6w HFD) or 12-week high-fat diet (12w HFD), respectively. Flow cytometry on digested atherosclerotic aortas enabled single-cell analysis of immune cell populations and a quantitative comparison of the HA-NP uptake in these cells (Figure 2B). In both groups, aortic macrophages displayed the highest median fluorescence intensity per cell (MFI) generated by Cy7-HA-NPs compared to both splenic and bone-marrow-resident macrophages (Figure 2B). These differences were, however, the most pronounced in the 6w HFD group; that is, the uptake of HA-NPs by the aortic macrophages was 6- and 40-fold higher compared to splenic and bone-marrow-resident macrophages, respectively. In contrast, fluorescent poly(lactic-*co*-glycolic acid (PLGA)-NPs, used as a control nanoformulation, displayed considerably higher uptake in splenic macrophages compared to aortic counterparts (Figure S5A, Supporting Information). Among the aortic immune cell populations, macrophages were found to engulf some PLGA-NPs (Figure S5B), albeit at lower levels than HA-NPs, indicative of the latter platform's favorable atherosclerotic plaque inflammation targeting features. Interestingly, we found dramatic differences in HA-NP uptake between macrophages in early and advanced aortic lesions; that is, MFI was 3060 ± 836 and 697 ± 142 au (arbitrary units), respectively (p = 0.000 03). These results coincide with our *in vitro* findings on the negative impact of oxLDL (Figure 2A) and suggest the occurrence of phenotypic changes in the macrophage population during disease progression. Early lesions are primarily composed of viable and freshly recruited macrophages, which display a high phagocytic activity. In contrast, the prolonged exposure to high cholesterol/lipid levels induces macrophage lipid overload and eventually cell apoptosis and necrosis. Other microenvironmental factors, such as oxLDL or reactive oxygen species, the concentrations of which are elevated in complex

DOI: 10.1021/acsnano.7b01385
ACS Nano 2017, 11, 5785−5799

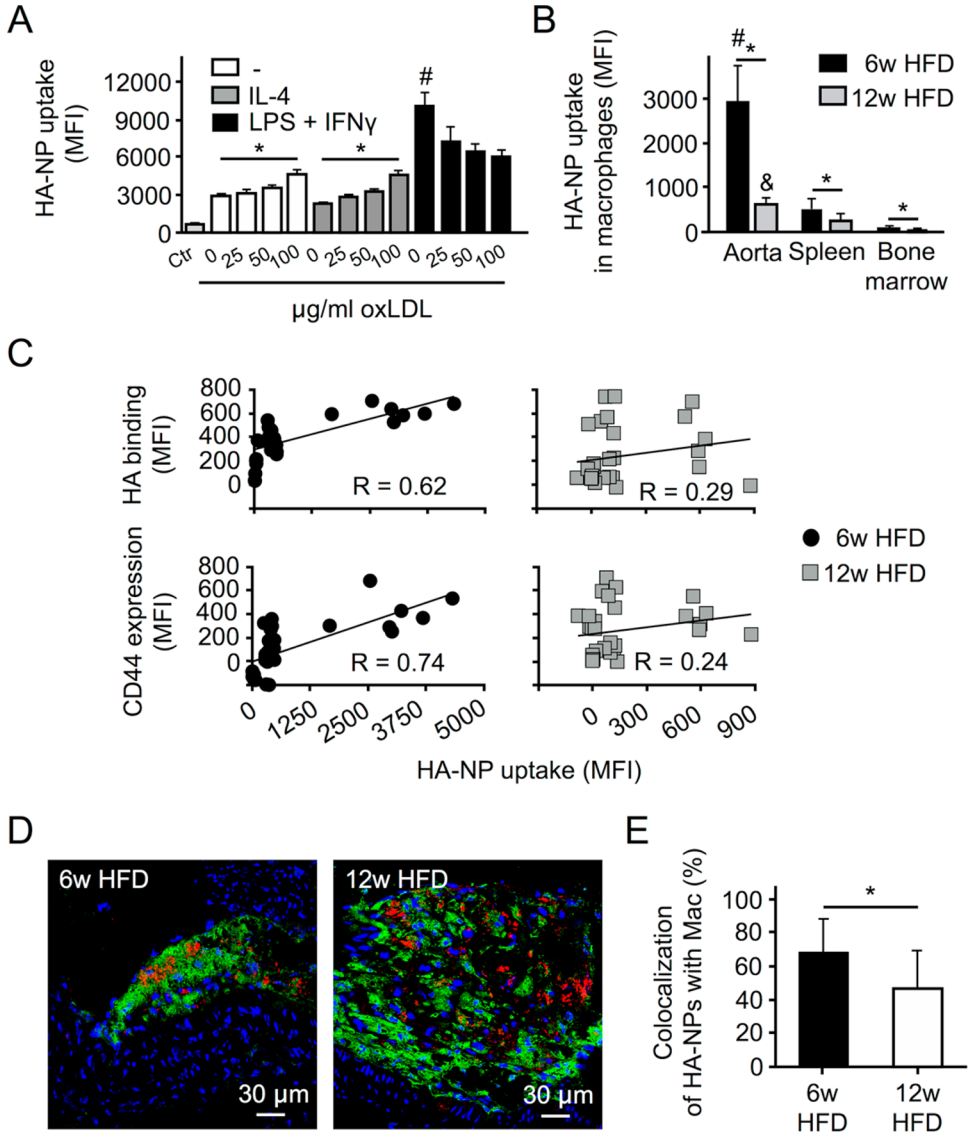

Figure 2. (A) Flow cytometry analysis of the cellular uptake of Cy5.5-labeled hyaluronan nanoparticles (HA-NPs) in different phenotypes of bone-marrow-derived macrophages. The macrophages are divided into three main phenotypic groups: naive (−) (white bars), interleukin 4 (IL-4)-stimulated (gray bars), and lipopolysaccharide (LPS) and interferon γ (INFγ)-stimulated (black bars). Moreover, three concentrations of oxidized low-density lipoprotein (oxLDL) were used for costimulation, *i.e.*, 25, 50, and 100 μg/mL. The cellular uptake of HA-NPs is expressed as the median fluorescence intensity per cell (MFI). Bars represent mean MFI/condition ± SD (ns = 3). Symbol "*" indicates a significant difference and "$^{\#}$" indicates significantly higher MFI compared to all other conditions at $p < 0.05$. (B) Uptake efficacy of Cy7-HA-NPs in aortic, splenic, and bone marrow macrophages measured by flow cytometry. Black and gray bars represent the data obtained for mice fed with a high-fat diet for 6 (6w HFD) and 12 weeks (12w HFD), respectively. Symbol "*" indicates intergroup differences, whereas "$^{\#}$" and "$^{\&}$" indicate significantly higher MFI compared to all other macrophage populations within the 6w HFD and 12w HFD groups, respectively, and at $p < 0.05$. (C) Scatter plots showing the relation between the uptake efficacy of HA-NPs and free hyaluronan (HA)-binding (upper panel) and expression of CD44 receptor (lower panel). All data were obtained by flow cytometry and are expressed as the median fluorescence intensity per cell. The correlations were investigated for pooled aortic leukocyte populations, *i.e*, macrophages, Ly6c^{high} and Ly6c^{low} monocytes, and neutrophils, in 6w HFD (left panel, black circles) and 12w HFD mice (right panel, gray squares). The black lines serve as guides for the eye. The correlation coefficient, *R*, was obtained from the nonparametric Spearman's correlation test. (D) Representative confocal microcopy images of aortic lesions detected in 6w HFD (left image) and 12w HFD group (right image). The Cy5.5-HA-NPs are shown in red, CD68 staining of macrophages is shown in green, and cell nuclei are blue. (E) Selectivity of HA-NPs toward plaque-associated macrophages expressed as the percentage of HA-NP-positive area that colocalizes with CD68-positive macrophage area. Bars represent mean ± SD. Symbol "*" represents significant difference at $p < 0.05$.

plaques, might also have negative effect on the macrophage activity.[56] A similar trend was observed for other immune cell populations in the aorta (Figure S6, Supporting Information) and, interestingly, in other tissues, including blood monocytes and splenic macrophages, which suggest a systemic effect of prolonged HFD. In line with our findings, the systemic immune effects of HFD have been described in the context of enhanced lipid loading of innate immune cells and their increased production.[57] We excluded the impact of instrumental error by monitoring MFI for unstained and stained control samples (Figure S7, Supporting Information).

Furthermore, we investigated the relation among HA-NP uptake in aortic immune cell populations, the efficacy to bind free

DOI: 10.1021/acsnano.7b01385
ACS Nano 2017, 11, 5785−5799

HA, and the expression of CD44 receptors. In the early atherosclerosis group, we found a significant correlation between HA-NP uptake and both HA-binding efficacy and CD44 expression, with Spearman's correlation coefficients of 0.62 and 0.74, respectively (both $p = 0.0001$) (Figure 2C). In mice with advanced lesions, the aforementioned parameters did not correlate. This suggests that initially the hyaluronan receptor–HA-NP interactions might play a role in the overall HA-NP uptake, which decreases during the disease progression.

Confocal microscopy analysis of mouse aortic arches confirmed the efficient uptake of HA-NPs in both early and advanced lesions (Figure 2D). However, based on the fraction of HA-NP-positive plaque area that colocalized with macrophage staining, we found a higher selectivity of HA-NPs toward macrophages in early atherosclerotic plaques, which was 67 ± 19% (Figure 2E). In advanced lesions, the macrophage selectivity was 46 ± 20%, which means that only this fraction of the total accumulated HA-NPs was engulfed by plaque macrophages and implies a considerably higher off-target accumulation of HA-NPs. We believe that this might be due to the impaired phagocytic activity of macrophages in advanced lesions (Figure 2B) and the presence of necrotic sites, which may facilitate passive accumulation of NPs.[58,59]

NP accumulation mechanisms in atherosclerotic plaques are rather scarcely explored.[60] Considering very limited neovascularization in mouse lesions, *i.e*, a microvascular fraction of *ca*. 1% based on our histological evaluation, the dysfunctional host endothelium seems to be a major player in NP plaque retention. This can occur *via* leaky endothelial junctions, which are formed in response to pro-atherogenic stimuli and a high tension induced by the subendothelial plaque deposition.[49,61,62] The leaky endothelial junctions have been proposed as a primary pathway of LDL accumulation in the vessel wall.[40] Alternatively, NPs might enter the plaques *via* the transcellular migration pathway, by exploiting intracellular vesicles.[63] As shown in Figure 1E,F, we could detect diffusely distributed HA-NPs in aortic endothelial cells. The subendothelial matrix is known to undergo degradation by the infiltrating macrophages, and therefore it does not create a physical barrier for NPs.

Atherosclerotic Plaque-Targeting, Circulation Kinetics, and Biodistribution of ^{89}Zr-HA-NPs in Mice. The accumulation of ^{89}Zr-HA-NPs in mouse atherosclerotic lesions was determined by autoradiography and gamma counting 24 h postadministration (Figure 3A,B). Both early and advanced atherosclerotic aortas displayed focal accumulation of radioactive material at typical sites of atherosclerotic plaque formation, *i.e*., aortic root, arch, and renal artery branching (Figure 3A). In contrast, the aortas of wild-type mice displayed low and homogeneously distributed radioactivity. Radioactivity quantification of excised aortas by gamma counting revealed a significantly higher percentage of injected dose (%ID) of ^{89}Zr-HA-NPs in atherosclerotic mice compared to their normal counterparts of approximately 30% (Figure 3B). Interestingly, despite a dramatic difference in disease stage, early lesions were equally well detectable as advanced plaques and displayed similar radioactivity concentrations. This was confirmed by *ex vivo* fluorescence imaging of aortas after injection of Cy5.5-HA-NPs (Figure S8, Supporting Information). This may be an important finding in view of the present challenges in the detection of early atherosclerosis.[64] In comparison, the previous studies on ^{18}F-FDG-PET, a method that probes cell metabolism, have shown an increasing metabolic activity associated with the atherosclerosis progression, which suggests an increasing inflammatory burden.[65,66] We believe that these discrepancies originate from the fact of assessing different aspects of macrophage activity. While macrophage glycolysis was shown to increase significantly in advanced lesions,[67] their phagocytic activity seems to undergo regression, as demonstrated by our flow cytometry (FACS) data (Figure 2A,B).

Furthermore, we studied the clearance kinetics of ^{89}Zr-HA-NPs by gamma counting of blood samples. In contrast to the previously reported fast clearance of radiolabeled hyaluronan,[19−21] ^{89}Zr-HA-NPs displayed biexponential decay kinetics with a short blood half-life ($t_{1/2,\alpha}$) of approximately 0.5 h and long $t_{1/2,\beta}$ of 9 h (Figure 3C). This might be due to the limited sensitivity of HA-NPs to the blood serum HYAL and/or decreased recognition by the hyaluronic acid receptor for endocytosis in the liver, which mediates systemic clearance of hyaluronan from the vascular and lymphatic circulation.[68] Nevertheless, we should also not rule out the impact of a relatively high HA-NP dose, which might lead to clearance saturation.[20] The quantitative determination of ^{89}Zr-HA-NP biodistribution in mice showed that the liver and spleen are the primary clearance organs of HA-NPs, containing between 10 and 20%ID/g (Figure S9, Supporting Information). The heart, which is an important organ in the context of human coronary atherosclerosis, displayed significantly lower %ID/g compared to the aorta. This suggests a potentially high target-to-background signal for PET imaging of coronary disease, which cannot be achieved by the clinically applied ^{18}F-FDG-PET since fluorodeoxyglucose is avidly taken up by myocardial cells.[69] In our study, we assume the *in vivo* integrity of HA-NPs and a fluorescent or radioactive label, which is based on the covalent conjugation and strong *in vitro* data on the nanoparticle stability. Nevertheless, we cannot reject the possibility of partial nanoparticle disintegration, which can occur under the *in vivo* conditions.[70]

PET Imaging of Rabbit Atherosclerosis with ^{89}Zr-HA-NPs. Subsequently, we investigated the performance of ^{89}Zr-HA-NP for PET imaging of atherosclerosis. Three rabbits were dynamically scanned on a PET/MRI scanner for 2 h after ^{89}Zr-HA-NP injection, as well as statically at 12 and 24 h postadministration. Representative PET/MRI fusion images are displayed in Figure 3D, on which we noninvasively monitored the circulation kinetics (Figure 3E) and time-dependent biodistribution (Figure 3F) of ^{89}Zr-HA-NPs. The initially high aortic PET signal, which was generated by the circulating ^{89}Zr-HA-NPs, decreased over time (Figure 3D,E). At 12 h postadministration, the aorta showed a relatively low but detectable PET signal, with some hot spots localized in the abdominal aorta (Figure 3G). The maximum standardized uptake values (SUV_{max}) were 6-fold higher for the aorta compared to the skeletal muscle ($p = 0.03$) (Figure 3G). The signal remained constant until 24 h postadministration. The clearance kinetics derived from PET images afforded a $t_{1/2}$ of approximately 3 h (Figure 3F). With respect to the biodistribution, assessed at 24 h postadministration by gamma counting, ^{89}Zr-HA-NPs reached the highest concentration of *ca*. 0.05%ID/g in the liver, spleen, kidney, and lungs, but considering the total organ mass, the liver and spleen were the primary clearance organs (Figure 3H). Similar to the mouse data, the heart tissue displayed very low radioactivity (~0.002%ID/g), which is desirable in context of the coronary atherosclerosis imaging. The confocal microscopy analysis of rabbit aortas confirmed the accumulation of Cy5.5-HA-NPs (showed in red) in the abdominal aorta, which underwent balloon injury, and

DOI: 10.1021/acsnano.7b01385
ACS Nano 2017, 11, 5785−5799

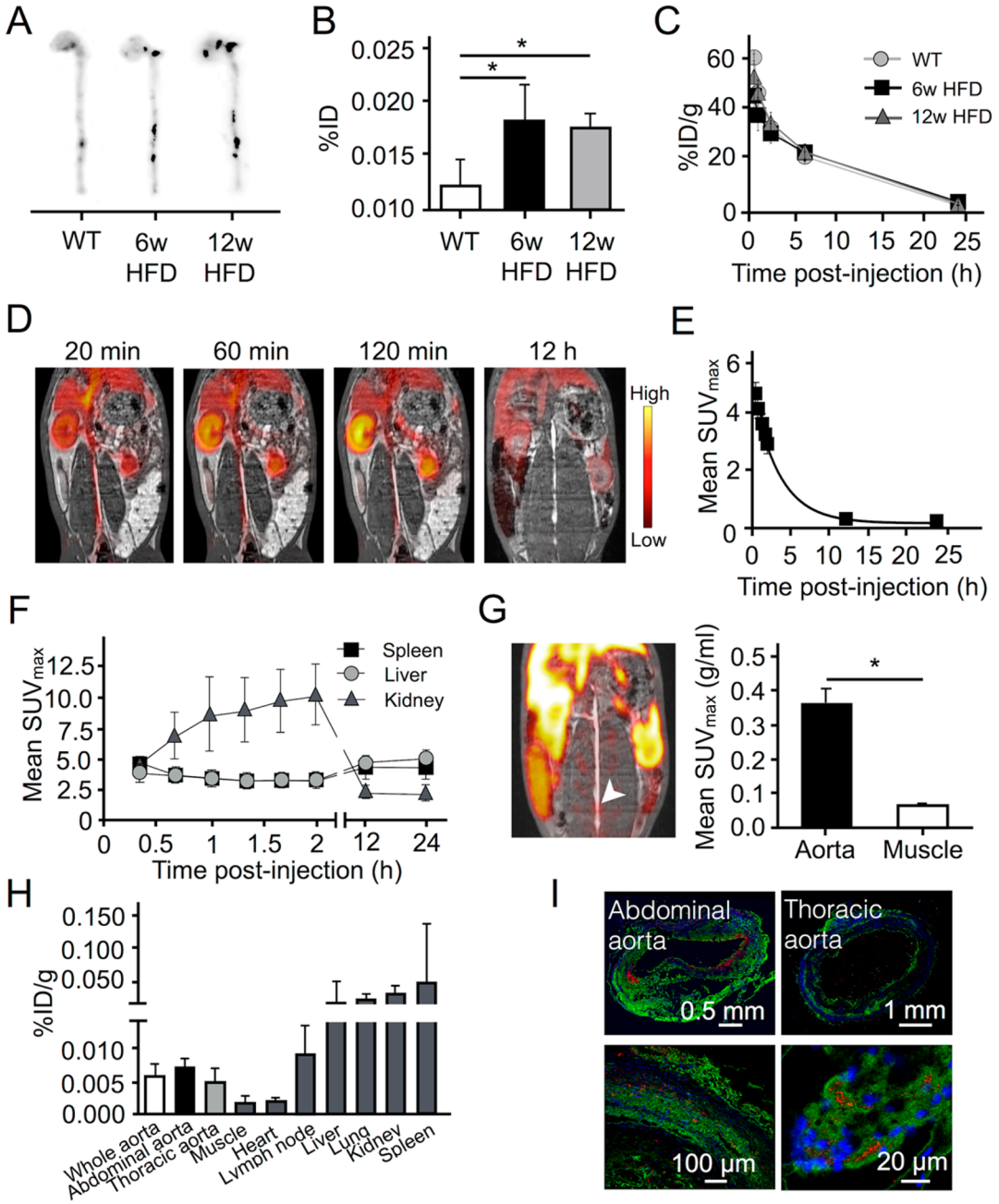

Figure 3. (A) Autoradiography images of aortas excised from a wild-type mouse (WT, left) and two atherosclerotic mice that were on a high-fat diet for either 6 weeks (6w HFD, middle) or 12 weeks (12w HFD, right). Twenty-four hours before sacrifice, the mice received intravenous injection of ^{89}Zr-HA-NPs. In the images, dark spots indicate higher radioactivity deposition. (B) Comparison between the radioactivity levels in healthy aortas (WT, white bar) and aortas with early (6w HFD, black bars) or advanced atherosclerosis (12w HFD, gray bars). The radioactivity was measured for the entire aorta by gamma counting 24 h after i.v. administration of ^{89}Zr-HA-NPs, and it is expressed as the percentage of injected dose (%ID). (C) Blood clearance kinetics of ^{89}Zr-HA-NPs determined by gamma counting in blood samples probed at different time points after NP injection. The data were obtained for the above-mentioned mouse groups and are presented as the mean ± SD of %ID per gram of blood (%ID/g) over time. (D) Coronal PET/MRI fusion images of an atherosclerotic rabbit, showing the organ radioactivity distribution at different time points after intravenous injection of ^{89}Zr-HA-NPs. (E) Clearance kinetics of ^{89}Zr-HA-NPs determined noninvasively in rabbits by measuring standardized uptake values (SUV) in the aortic blood. (F) Time-dependent biodistribution of ^{89}Zr-HA-NPs determined by dynamic (20 min to 2 h) and static (12 and 24 h) PET imaging in the spleen (black squares), liver (gray circles), and kidney (gray triangles). (G) Left panel displays a representative PET/MRI fusion image of an atherosclerotic rabbit 12 h after the administration of ^{89}Zr-HA-NPs. PET signal hot spot can be observed in the abdominal aorta (white arrowhead). In the right panel, the bar chart shows the difference between SUV of the aorta and skeletal muscle at 12 h postinjection. (H) Biodistribution of ^{89}Zr-HA-NPs in different rabbit organs quantified *ex vivo* by gamma counting and presented as %ID/g of tissue. (I) Confocal microscopy images of the abdominal (upper left) and thoracic aorta (upper right) from a rabbit that was co-injected with both ^{89}Zr-HA-NPs and Cy5.5-HA-NPs. The Cy5.5-HA-NPs are displayed in red, RAM-11 staining of macrophages is shown in green, and cell nuclei are blue. In the lower panel, higher magnification images of abdominal aorta show the engulfed HA-NPs by macrophages. In all bar charts, bars represent mean ± SD and symbol "*" indicates the significant difference at $p < 0.05$.

DOI: 10.1021/acsnano.7b01385
ACS Nano 2017, 11, 5785−5799

no detectable NP fluorescence in the untreated thoracic aorta (Figure 3I). In the abdominal aorta, HA-NPs were localized in macrophage-rich areas and were internalized by aortic macrophages (Figure 3I, lower image panel).

The aforementioned results underline the translational aspect of our study. We applied a ^{89}Zr-deferoxamine (DFO)-labeling strategy, which assures an excellent match between nanoparticle biological half-life and ^{89}Zr physical half-life[71] and which we previously demonstrated in lipid- and polymer-based nanoparticle systems.[72,73] We showed that HA-NPs can be effectively labeled with ^{89}Zr-DFO and enable the detection of atherosclerosis in two animal models, also at the early disease stage. The imaging studies that exploited hyaluronan-mediated targeting of atherosclerosis are scarce.[74−76] Previously, only Lee *et al.*[76] based their nanoformulation on HA and proposed the fluorescence imaging of atherosclerosis. We, however, provide in-depth analysis of the underlying HA-NP−immune cell interactions and a strong translational aspect by employing noninvasive PET/MRI.

Our study shows also some interspecies differences between the mice and rabbits regarding HA-NP kinetics and biodistribution. In mice, ^{89}Zr-HA-NPs displayed biexponential decay kinetics, which has been previously attributed to the nanoparticle size heterogeneity; that is, larger nanoparticles are more rapidly cleared from the circulation compared to smaller counterparts.[77] Moreover, a different clearance mechanism needs to be considered. Our FACS data indicate a growing involvement of blood phagocytes in the clearance of HA-NPs over time postadministration, as shown in Figure S10A (Supporting Information) in blood samples taken 15 min and 2 h postinjection. Furthermore, we observed a shift in the monocyte population toward the Ly6c^{high} phenotype (Figure S10B). Possibly, the fast clearance phase is driven by the nanoparticle filtration by the reticuloendothelial system, while in the slow phase, HA-NPs might be predominantly associated with the blood-circulating phagocytes. In rabbits, displaying monoexponential clearance kinetics of ^{89}Zr-HA-NPs, these mechanisms were not investigated.

With respect to the biodistribution, we report very different retention values of a total dose per gram of mouse and rabbit organs. These differences originate from the fact that we normalize the organ radioactivity to the total injected dose and organ weight. However, the organ weights of a mouse and New Zealand White rabbit differ dramatically; for example, for the liver, it is ∼1−1.5 and ∼140−150 g, respectively. Therefore, 10%ID/g of a mouse tissue represents practically a full organ retention, while 0.05%ID/g of a rabbit liver represents a dose retention in only a small fraction of this organ. Please note that the relative differences between the organs' radioactivity are rather similar in both mice and rabbits.

Hyaluronan Nanoparticles Improve the Atherosclerotic Plaque Stability in Atherosclerotic Mice. In view of the previously reported anti-inflammatory activity of high-molecular-weight HA,[10] we hypothesized that HA-NPs, composed of megadalton HA aggregates, may also exert anti-inflammatory effects. To test this hypothesis, we studied the effects of HA-NPs on atherosclerosis in *apoe*$^{-/-}$ mice, which received weekly injections of HA-NPs for 12 weeks. The effects were compared to free 75 kDa HA (free HA), which served as a substrate for the nanoparticle formulation, and phosphate-buffered saline (PBS, control).

Histological evaluation of aortic roots involved the assessment of mean plaque area and plaque composition (macrophages and collagen) (Figure 4A). The HA-NP-treated mice displayed the most favorable plaque phenotype regarding all the aforementioned parameters. The lesions were significantly smaller compared to the control group and contained approximately 30% fewer macrophages compared to both the control and free HA-treated mice. Moreover, they displayed 30−40% higher collagen content, which is an important factor for plaque stability.[78] The anti-inflammatory effects of HA-NPs were confirmed by flow cytometry analysis of aortic arches (Figure 4B) and by CD45 staining of aortic roots (Figure S11, Supporting Information). Both methods revealed a ∼30−50% lower number of immune cells in the HA-NP-treated mice compared to both free HA-treated and control mice. At the same time, we found no systemic immune effects of HA-NPs, as deduced from the analysis of blood, spleen, and bone marrow (Figure S12, Supporting Information).

We show that nanoparticle-formulated hyaluronan exerted anti-inflammatory activity, which was previously attributed exclusively to high-molecular-weight linear hyaluronan (HMW-HA).[10] While the application of high-viscosity HMW-HA in the treatment of atherosclerosis is limited by the necessity of local administration,[79] our formulation displays favorable blood circulation kinetics (Figure 3C,E) and selectivity toward pro-inflammatory/plaque-associated macrophages (Figure 2A,B). Previously developed HA-containing NPs induced therapeutic effects *via* other key-acting therapeutic agents, while exploiting HA as a targeting moiety.[29,80] A possible mechanism of HA-NP atheroprotective activity involves a direct interaction of HA-NPs with macrophages/monocytes, which might lead to the downregulation of inflammatory response. This has been previously described for HMW-HA,[10] and, in our study, it is implied by the reduced immune cell infiltrates and higher collagen content (Figure 4). In line with this hypothesis, our *in vitro* study in bone-marrow-derived macrophages showed that a high concentration of HA-NPs significantly inhibited production of nitric oxide (NO) and tumor necrosis factor (TNF), the key pro-inflammatory mediators (Figure S13, Supporting Information). A similar trend was observed for the pro-inflammatory interleukins IL-6 and IL-12. In contrast, oligomeric HA had no significant effect on the expression on NO or TNF, while it significantly increased the IL-6 and IL-12 production. Interestingly, we also observed a significant stimulatory effect of HA-NPs on the expression of arginase-1 gene (Arg-1), which is considered as an important marker of pro-fibrotic macrophages and its overexpression may contribute to atherosclerotic plaque stability. Concurrently, we anticipate a potential impact of long circulating HA-NPs on the vascular glycocalyx, which is predominantly composed of hyaluronan.[81] HA-NPs might serve as a circuiting reservoir of hyaluronan and be "built into" the glycocalyx, which, in consequence, might limit the immune cell infiltration into the lesion site.

CONCLUSIONS

We have developed highly biocompatible HA-NPs as a platform for imaging and therapy of atherosclerosis. In our nanoformulation, hyaluronan serves as both the primary building block and the targeting/bioactive molecule, which yields high morphological stability of HA-NPs under hydrolytic conditions. HA-NPs are preferentially taken up by pro-inflammatory macrophages *in vitro* and display high selectivity toward atherosclerotic plaque-associated macrophages in mice. Interestingly, we found that the efficacy of macrophage−HA-NP interactions is strongly dependent on the disease stage, which we attribute to phenotypic dynamics of macrophage population. Furthermore, we showed that radiolabeled HA-NPs target mouse atherosclerotic lesions

DOI: 10.1021/acsnano.7b01385
ACS Nano 2017, 11, 5785−5799

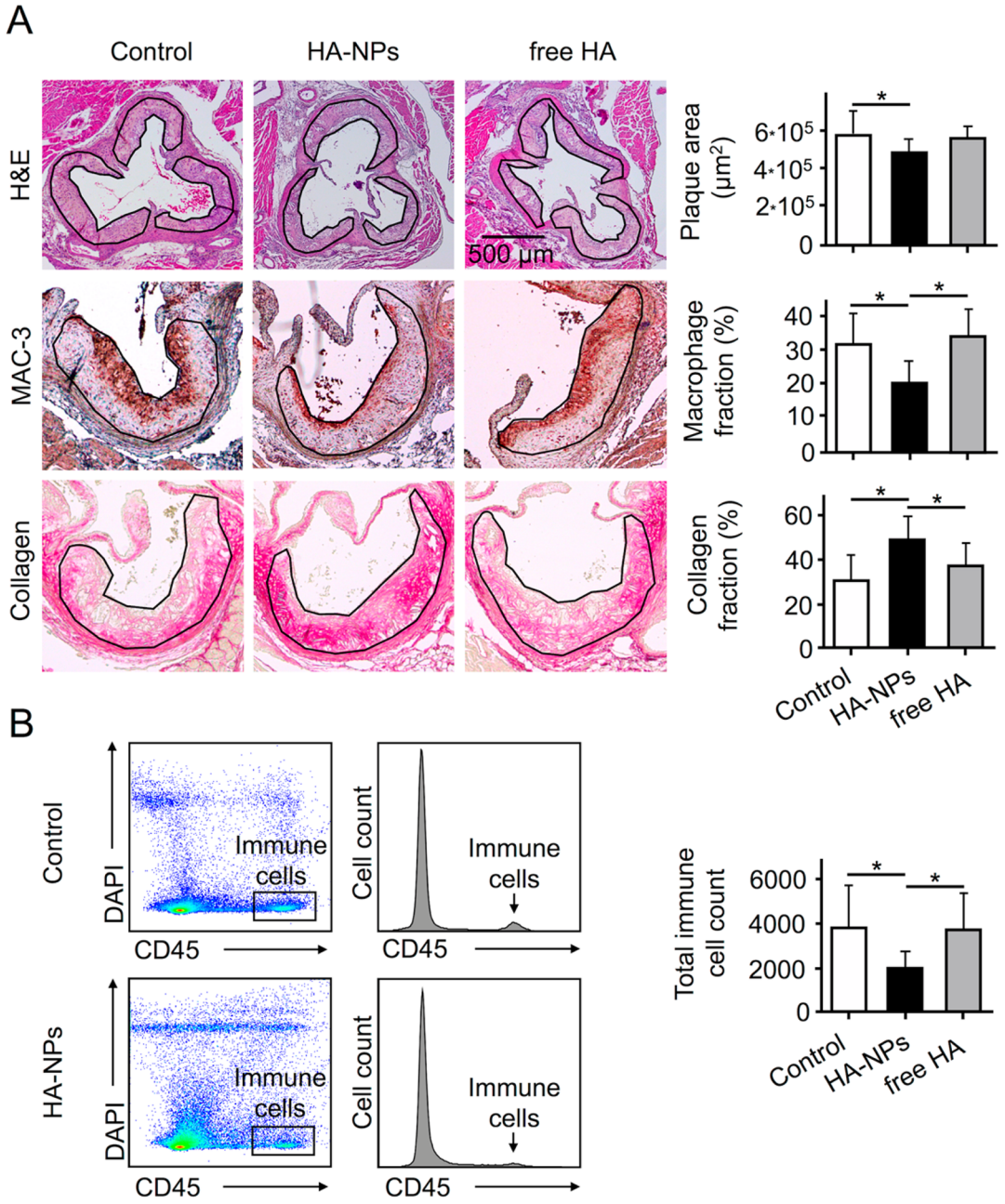

Figure 4. (A) Representative images of aortic roots from mice that received either PBS (control, left image panel), HA-NPs (middle image panel), or free HA (right image panel) during a 12-week high-fat feeding period. The sections were stained with hematoxylin and eosin (H&E), macrophage-specific antibody (MAC-3), or sirius red (collagen). Scale bar in the upper right image refers to all H&E-stained sections. Bar charts display the mean plaque area (top), percentage of plaque area containing macrophages (middle), and collagen (bottom) in the aforementioned treatment groups. (B) Flow cytometry analysis of aortic arches of the treated mice. Left panel shows representative cell scatter plots and histograms obtained for a control (upper panel) and HA-NPs-treated mouse (lower panel). The immune cells are defined as CD45-positive cells. Bar chart compares the total immune cell count in the control, HA-NPs-treated, and free HA-treated mice. In all bar charts, bars represent mean ± SD and symbol "*" indicates the significant difference at $p < 0.05$.

and enable PET imaging of atherosclerosis in rabbits. Finally, we demonstrated that HA-NPs exert atheroprotective effects by decreasing the immune cell infiltration in aortic lesions.

METHODS

Hyaluronan Nanoparticle Preparation. Hyaluronan (66–99 kDa) was purchased from Lifecore Biomedical (Chaska, MN, USA). A 200 mg of HA was dissolved in 10 mL of 2-(*N*-morpholino)ethanesulfonic acid (MES) buffer (Sigma-Aldrich, Zwijndrecht, The Netherlands) pH 6 and activated with 92 mg of 1-ethyl-3-(3-(dimethylamino)propyl)carbodiimide hydrochloride (EDC) (Thermo Fisher Scientific, Ermelo, The Netherlands) and 104 mg of *N*-hydroxysulfosuccinimide (sulfo-NHS) (Thermo Fisher Scientific). EDC and sulfo-NHS were dissolved in 200 μL of MES buffer pH 6 and added sequentially to HA solution during stirring, with 15 min intervals. Subsequently, the pH was adjusted up to 7 using 5 M NaOH, 128 μL of ethylenediamine (Sigma-Aldrich) was added, and the pH was rapidly adjusted down to 7 using 5 M HCl. The reaction mixture was stirred at room temperature overnight. The amine-functionalized HA ($HA\text{-}NH_2$) was purified by dialysis against water (Spectra/Por 2 membrane, 12–14 kDa cutoff, Spectrum Laboratories, Breda,

DOI: 10.1021/acsnano.7b01385
ACS Nano 2017, 11, 5785–5799

The Netherlands) and four series of ethanol precipitation (3 volumes ethanol:1 volume water). To induce HA precipitation, NaCl (Sigma-Aldrich) was added to the postdialysis water solution of HA to obtain a final concentration of 5% NaCl. Subsequently, 3 parts of ethanol was added, and the mixture was shaken vigorously until a white precipitate appeared, which was pelleted by centrifugation at 4000 rpm for 20 min. The supernatant was removed by careful pipetting, and the HA-NH_2-containing pellet was redissolved in ultrapure water. For a subsequent series of ethanol precipitation, NaCl was added and the process was repeated. After the fourth ethanol precipitation, the HA pellet was dissolved in ultrapure water, dialyzed against water overnight, and freeze-dried (Zirbus VaCo2-II, Zirbus, Bad Grund, Germany). The dry lyophilizate was weighed (the average yield was 70−80%) and analyzed with respect to the amine content. The number of primary amines per HA molecule was 6−12, as determined by the 2,4,6-trinitrobenzenesulfonic acid assay (Thermo Fisher Scientific).

In the second step, cholanic NHS ester was prepared by reacting 30 mg of cholanic acid with 17 mg of *N*,*N*′-dicyclohexylcarbodiimide (*i.e*, 83 μL of a 1 M solution) (Thermo Fisher Scientific) and 13 mg of *N*-hydroxysuccinimide in dry dimethylformamide (DMF) (all aforementioned chemicals were from Sigma-Aldrich). First, cholanic acid was dissolved in 400 μL of DMF, and 83 μL of *N*,*N*′-dicyclohexylcarbodiimide solution was added, which was followed by vortexing. Next, *N*-hydroxysuccinimide was dissolved in ∼50 μL of DMF and added to the reaction mixture, which was vortexed again. The reaction was allowed to sit overnight at room temperature without stirring. The precipitate of the urea derivative, which is a byproduct of the reaction, was removed by centrifugation at 10 000 rpm for 10 min. The supernatant was aspired carefully from above the pellet and was used for further reaction. The supernatant containing a 6 mol excess of cholanic ester was added drop by drop to the solution of HA-NH_2 in 0.1 N $NaHCO_3$ pH 9 (20 mg/mL). The reaction was stirred overnight at room temperature, and its product was purified by dialysis against water and filtration. Subsequently, the material was freeze-dried, weighed, and stored at −20 °C.

Fluorescence Labeling of Hyaluronan Nanoparticles. Fluorescent hyaluronan nanoparticles were prepared by conjugating an NHS derivative of a fluorescent dye to the residual primary amino groups on the nanoparticles. First, HA-NPs were dispersed in 0.1 N $NaHCO_3$ pH 8.5 at a concentration of 10 mg/mL, added to a DMF solution of either Cy5.5- or Cy7-NHS ester (Lumiprobe GmbH, Hannover, Germany) (60% water-based buffer: 40% DMF), and stirred for 4 h at room temperature. An 8 mol amount of dye was added per 1 mol of residual NH_2 group. The unreacted dye was removed by ethanol precipitation (four times or until the supernatant was clear) and dialyzed against water for 24 h. The labeling resulted in approximately 0.2 mol dye/mol of HA, based on absorbance measurements.

Radiolabeling of Hyaluronan Nanoparticles. HA-NPs were modified with deferoxamine B to enable radiolabeling with zirconium-89 (^{89}Zr). p-SCN-Bn-DFO (Macrocyclix, Plano, TX, USA) in DMSO (5 mg/mL) was added to a nanosuspension of HA-NPs in 0.1 M carbonate buffer (pH 8.9) (10 mg/mL) in steps of 5 μL until a 2-fold molar excess over residual amine groups of NP-incorporated HA. The reaction mixture was vortex-mixed after each addition and then shaken at 37 °C for 4 h. The DFO-modified nanoparticles (HA-NPs-DFO) were purified by spin filtration using a 10 kDa molecular weight cutoff (MWCO) (Sartorius Stedim Biotech GmbH, Goettingen, Germany) and washing four times with fresh PBS. The final retentate was diluted with PBS to achieve a final HA concentration of 5 mg/mL. The HA-DFO nanoparticles were reacted with ^{89}Zr oxalate in PBS (pH 7.4) for 2 h at 37 °C. Radiolabeled HA nanoparticles (^{89}Zr-HA-NPs) were separated from unreacted ^{89}Zr by centrifugal filtration using a 10 kDa MWCO and washing with sterile PBS. The radiochemical yield was 94 ± 1% (n = 3), and the radiochemical purity was >98% as determined by size exclusion chromatography. The number of DFO labels per HA molecule was measured to be ∼1 by the isotope dilution method.

Animal Experiments. *Mice.* Eight-week-old *apoe*$^{-/-}$ mice (Charles River Laboratories) were fed with a high-fat diet (TD.88137, Envigo, Alconbury Huntington, UK) for either 6 or 12 weeks to induce early and advanced atherosclerotic lesions, respectively. The wild-type mice served as negative controls. After the diet period, the mice received an injection of HA-NPs (25 mg/kg), which were labeled with either a fluorescent dye or radiotracer, *via* the tail vein. Twenty-four hours after injection, the mice were sacrificed and perfused with PBS, and aortas with other organs were removed and underwent different examinations. The entire aorta with aortic roots, spleen, blood, and bone marrow from mice that received Cy7-HA-NPs (n = 7) were analyzed by flow cytometry. The immunohistochemical analysis of aortic arches was performed in mice that were administered with Cy.5.5-HA-NPs (n = 5). The organs from ^{89}Zr-HA-NPs-injected mice were analyzed by autoradiography and gamma counting (n = 4).

In the therapeutic study, 8-week-old *apoe*$^{-/-}$ mice on a high-fat diet received once a week for 12 weeks an intravenous injection of either HA-NPs, free HA (both 50 mg/kg/week), or PBS (ns = 10). After 12 weeks of treatment, the mice were sacrificed and aortas perfused with cold PBS. The excised aortic arch and descending aorta including the renal arterial branching were analyzed by flow cytometry, whereas aortic roots were analyzed by histology.

All mouse experiments were performed in accordance with protocols approved by the Animal Experiment Committee of Academic Medical Center in Amsterdam or Institutional Animal Care and Use Committee of Mount Sinai School of Medicine (MSSM) in New York.

Rabbits. Three male New Zealand White rabbits (2.5−3.0 months old) were purchased from Charles River Laboratories (Wilmington, MA, USA). To induce the formation of atherosclerotic plaques, endothelial denudation of the aorta was performed by angioplasty. Animals were anesthetized after an intramuscular (i.m.) administration of ketamine (20 mg/kg) (Fort Dodge Animal Health, Overland Park, KS, USA) and xylazine (5 mg/kg) (Bayer AG, Leverkusen, Germany). A 4F-Fogarty embolectomy catheter (Edwards Lifesciences, Irvine, CA, USA) was introduced in the femoral artery, ascended up to the level of the left subclavian artery, and inflated until a pressure of 2 atm was established. Next, the balloon was slowly deflated while retracting until the iliac bifurcation was reached, all performed under X-ray guidance using a clinical cardiovascular intervention Philips system (Allura Xper FD20/10, Philips Healthcare, Best, The Netherlands). The procedure was repeated using the contralateral femoral artery as point of entry, 4 weeks after first procedure and 6 weeks after the initiation of a high cholesterol diet, composed of regular chow diet enriched with 0.3% cholesterol and 4.7% coconut oil (Research Diets, Inc. Brunswick, NJ, USA). After 8 weeks, the diet was changed to 0.15% enriched cholesterol with 4.7% coconut oil diet and continued for the remainder of the experiment. The rabbit experiments were performed in accordance with protocols approved by the Institutional Animal Care and Use Committees of MSSM and followed National Institutes of Health guidelines for animal welfare.

Flow Cytometry of Mouse Tissues. Flow cytometry (FACS) measurements were performed to determine the targeting properties and immune effects of HA-NPs in *apoe*$^{-/-}$ mice. Twenty-four hours after Cy7-HA-NP administration (targeting study) or 12 weeks after HA-NP therapy (therapeutic study), the mice were sacrificed and blood was collected by cardiac puncture. Subsequently, the mice were perfused with cold PBS, and the entire aorta, including roots, was excised. After 1 h digestion in 4 U/mL Liberase (Roche Life Sciences, Almere, The Netherlands), 60 U/mL hyluronidase (Sigma-Aldrich), and 40 U/mL DNase I (Sigma-Aldrich) of PBS solution at 37 °C, the aorta digests were resuspended, filtered through the cell strainer (Fisher Scientific), and washed three times with FACS buffer (1% BSA in PBS). The spleen was homogenized manually and strained through the cell strainer, whereas bone marrow was flushed out from the femur bone by using cold PBS and resuspended into a single-cell suspension by using a 26G needle. Subsequently, the blood, spleen, and bone marrow underwent erythrocyte lysis (eBioscience, San Diego, CA, USA) and were washed three times with FACS buffer.

The cell suspensions from all the organs were stained for FACS analysis. First, the mouse Fc block (BD Pharmingen, Breda, The Netherlands) was added. Ten minutes thereafter, the antibody cocktail was introduced. The following anti-mouse antibodies were used for FACS staining of mice injected with Cy7-HA-NPs: Brilliant Violet 510-CD45, Brilliant Violet 711-CD11b (both BioLegend, San Diego,

DOI: 10.1021/acsnano.7b01385
ACS Nano 2017, 11, 5785−5799

CA, USA), FITC-F4/80 (CI:A3-1) (Bio-Rad, Oxford, UK), PE-CF594-Ly6c (AL-21) (BD Pharmingen), Brilliant Violet 650-CD44 (IM7). All the antibodies were diluted to 1:200 with FACS buffer. DAPI (ThermoFisher Scientific) was used at a concentration of 2 μg/mL for dead cell staining. Moreover, we prepared fluorescently labeled hyaluronan to determine the hylaronan-binding efficacy by different immune cell populations. In short, HA (60−90 kDa) was dissolved in PBS buffer pH 7.2 and reacted with EDC and sulfo-NHS (both ThermoFisher Scientific) at room temperature while stirring (quantities are given in the section on HA-NP preparation). After 0.5 h, an 8 molar excess of disulfo-Cy5-hydrazide (Cyandye, Sunny Isles Beach, FL, USA) in PBS pH 7.2 was added to the EDC- and sulfo-NHS-reacted HA and stirred for 4 h at room temperature. The reaction product, Cy5-HA, was purified by dialysis and ethanol precipitation (four times). For FACS staining, 50 μg/mL of Cy5-HA was used in a cocktail with the aforementioned antibodies. The cell suspensions were incubated with antibodies and Cy5-hyaluronan for 30 min and washed three times with FACS buffer.

The FACS staining of mouse material from the therapeutic study included the following antibodies: Pacific Blue-conjugated NK-1.1, CD90.2, Ly-6G, TER-119, CD49b and CD45R/B220, Brilliant Violet 510-CD45, PE-CD11b, FITC- Ly6c (AL-21), PE-Cy7-F4/80 (CI:A3-1), and Cy5-HA (custom-made). All the antibodies were purchased from BioLegend and used at a dilution of 1:200 excluding FITC-Ly6c, which was diluted 1:100.

FACS measurements were performed on either a BD LSRFortessa (BD Biosciences) (targeting study) or a BD LSR II (BD Biosciences) (therapeutic study). The obtained data were analyzed with FlowJo V10 software (FLOWJO, Ashland, OR, USA). The macrophages, monocytes, and neutrophils were defined according to the gating strategy presented in Figure S6A (Supporting Information). For these cell populations, the uptake of Cy7-HA-NPs was determined and expressed as median fluorescence intensity per cell. Furthermore, the MFIs of Brilliant Violet 650-CD44 and Cy5-HA were used as quantifiers of CD44 expression and HA-binding efficacy, respectively. The analysis of FACS data obtained from mice that underwent a 12-week treatment was limited to the assessment of total immune cell population (CD45-positive), which was due to overall low cell numbers obtained from aortic arches.

Autoradiography of Mouse Aortas. The perfused and excised aortas were placed in a film cassette against a phosphorimaging plate (BASMS-2325, Fujifilm, Valhalla, NY, USA) for 72 h at −20 °C to determine the radiotracer distribution. Phosphorimaging plates were read at a pixel resolution of 25 μm with a Typhoon 7000IP plate reader (GE Healthcare, Pittsburgh, PA, USA). The images were postprocessed using ImageJ software.

Pharmacokinetics and Biodistribution in Mice. Gamma counting was used to assess the biodistribution and clearance kinetics of ^{89}Zr-HA-NPs and performed on a Wizard^2 2470 automatic gamma counter (PerkinElmer, Waltham, MA, USA). First, the injection samples of ^{89}Zr-HA-NP were measured to determine the total injected dose of radioactivity (ID). Two minutes, 30 min, 2 h, 6 h, and 24 h postadministration, small blood samples were taken from the lateral tail vein. At 24 h after injection of ^{89}Zr- HA-NPs, the mice were sacrificed and the aorta, liver, spleen, kidneys, lung, heart, and a part of the femoral muscle were collected. The radioactivity of each sample was measured and normalized to the ID and sample weight and expressed as the percentage of ID that was retrieved in one gram of tissue (%ID/g). For statistical comparison of aortas, the aortic radioactivity was normalized to the ID only and expressed as the percentage of injected dose.

To determine the blood clearance parameters, the blood radioactivity data were fitted by a mono- and biexponential decay model. The best fitting model, as concluded from the correlation coefficient, r^2, was used for reporting. The same strategy was used for the rabbit data.

Immunohistochemistry of Mouse Tissues. The mouse aortic arches were embedded in Tissue-Tek O.C.T. (Sakura; Alphen aan den Rijn, The Netherlands) and frozen in 2-methylbutane (Sigma) on dry ice. Subsequently, they were cut into 7-μm-thick sections and fixed with ice-cold acetone for 5 min. Before staining, they were blocked with 5% fetal calf serum (FCS) in PBS for 60 min. Next, the sections were incubated overnight at 4 °C with rat anti-mouse CD68 primary antibody (AbD Serotec; 1:200 dilution; clone: FA-11). After washing, Alexa Fluor 488-conjugated donkey anti-rat IgG secondary antibody (Thermo Fischer Scientific; 1:500 dilution) was applied for 1 h. Nuclei were stained with DAPI.

The images of stained aortic arches were acquired using a Leica TCS SP8 confocal microscope (Leica Microsystems) at 400× magnification. On average, we imaged four different plaque areas in each arch section, while imaging six tissue sections per mouse. The obtained images were analyzed using Leica LAS-X software. First, we defined the plaque area, which was used as a normalizing parameter. Furthermore, we determined the area positive for Alexa Fluor 488-CD68 (macrophage staining) or HA-NPs-Cy5.5. This was done by applying a threshold to the appropriate fluorescence channel and creating a mask, which was used to calculate the fluorescence-positive area. Furthermore, the area of colocalization of Alexa Fluor 488-CD68 with HA-NPs-Cy5.5 was determined. Subsequently, we calculated the percentage of HA-NP-positive area that colocalizes with macrophage staining, which was used as an indication of the HA-NP selectivity toward plaque-associated macrophages.

To determine the effects of HA-NP treatment on the atherosclerotic plaque development, the mouse hearts with aortic roots were fixed in 4% paraformaldehyde (Sigma-Aldrich) and embedded in paraffin, after the process of dehydration. The aortic roots were cut into 7-μm-thick sections and stained with (1) hematoxyline and eosin (H&E); (2) rat anti-mouse MAC-3 antibody (clone M3/84; BD Pharmingen; 1:30 dilution; overnight incubation), followed by rabbit anti-rat biotinylated secondary antibody (Vector Laboratories, Burlingame, CA, USA; 1:300 dilution, 30 min incubation) and avidin-peroxidase (Vectastatin Elite ABC HRP Kit, Vector Laboratories), color was induced with ImmPact AMEC red peroxidase substrate (Vector Laboratories); and (3) sirius red staining (Sigma-Aldrich) (collagen staining). The stained tissues were analyzed with a light microscope (Leica) at 50× magnification. The mean plaque area was assessed from H&E-stained sections. This was done by delineating plaque areas in 5−6 root sections/mouse. The selected sections had to contain all three aortic valves. The average of all measurements was used as the mean plaque area. The fractions of macrophage and collagen area were assessed in a similar manner. First, the total plaque area was delineated and calculated. The further image analysis included only the plaque area. Color images were transformed into gray-scale images. Subsequently, a threshold was set to select only high-intensity pixels and create binary image. From the latter, the threshold-limited area was calculated and normalized to the total plaque area. All the aforementioned image analyses were performed using Fiji software.[82]

PET/MR Imaging in Rabbits. Rabbits (n = 3, weight: 3.6 ± 0.4 kg) received a 24G-catheter in the right marginal ear vein for injection with ^{89}Zr-HA-NPs and Cy5.5-HA-NPs (1.40 ± 0.02 mCi; ∼25 mg total HA). Anesthesia was induced by an intramuscular injection of ketamine (20 mg/kg) (Fort Dodge Animal Health), combined with xylazine (0.5 mg/kg) (Bayer, Shawnee Mission, KS, USA). Before scanning, all rabbits received a urine catheter to prevent any disruptions from signals in the bladder and were placed in a body matrix coil. During scanning, rabbits received isoflurane anesthesia at 1.5% by inhalation and were oxygenated for the remainder of the PET/MR imaging experiment, while vital parameters were monitored.

Shortly after ^{89}Zr-HA-NPs injection, images were acquired in a dynamic fashion for the duration of 2 h using a clinical 3 T PET/MRI Biograph mMR (Siemens, München, Germany). Attenuation correction of PET images was done using the built-in two-point Dixon MR-based attenuation correction (MR-AC) map, and images were reconstructed using the OP-OSEM algorithm. After scout scans, the PET scan was initiated and acquired simultaneously with bright-blood time-of-flight (TOF) noncontrast enhanced angiography performed for localization of arterial anatomical landmarks (renal arteries and iliac bifurcation). Imaging parameters were as follows: TR, 23 ms; TE, 2.8 ms; flip angle, 20 degrees; spatial resolution, 0.35 mm^2 (interpolated); slice thickness, 1 mm. Simultaneously a black blood 3D T2 weighted sampling perfection with application optimized contrasts using different flip angle evolution (SPACE) sequence was used for vessel wall delineation.

DOI: 10.1021/acsnano.7b01385
ACS Nano 2017, 11, 5785−5799

Imaging parameters were as follows: TR, 1600 ms; TE, 115 ms; flip angle, 120 degrees; echo train length, 83; spatial resolution, 0.63 mm^2; slice thickness, 0.63 mm. Static PET scans were performed at 12 ± 1.8 and 24 ± 0.1 h after injection, using a TOF and MR-AC as described above.

Analysis of PET images was performed after all data were processed and divided in different time frames using a custom-made program written in Matlab (MathWorks, Natick, MA, USA). All data was subsequently processed with OsiriX imaging software (Pixmeo SARL, Bernex, Switzerland) by drawing regions of interest (ROIs) on the infrarenal abdominal aorta and major organs (liver, spleen, and kidneys). By averaging all acquired ROIs per organ (≥10 per organ), mean standardized uptake values (mean SUV_{max}) (g/mL) for each target tissue were obtained.

Pharmacokinetics and Biodistribution in Rabbits. Radioactivity half-lives were determined by drawing blood from the ear arteries at 1 and 30 min and at 1, 2, 12, and 24 h postinjection. All rabbits were sacrificed by an i.v. injected overdose of 100 mg/kg sodium pentobarbital and flushed afterward with a bolus of heparinized saline. All rabbits were pinched in the feet to check for reaction prior to systemic perfusion with at least 500 mL of saline solution. Aortas were excised and divided into thoracic and abdominal aorta, the latter with celiac trunk and renal arteries attached, serving as landmarks. The following organs were harvested: heart, lungs, liver, spleen, kidneys, para-aortic lymph node, and muscle. All tissues were weighed before counting with a Wizard^2 2480 automatic gamma counter (PerkinElmer).

Immunohistochemistry of Rabbit Aorta. From rabbits that were co-injected with ^{89}Zr- and Cy5.5-labeled HA-NPs, several samples of abdominal and thoracic aorta were collected. The samples were frozen in Tissue-Tek O.C.T. (Sakura) and cut into 7-μm-thick sections. Before staining, they were fixed for 5 min in ice-cold acetone. After blocking with 4% FCS, the aortic sections were stained with a mouse anti-rabbit macrophage antibody (RAM-11, Dako, Heverlee, Belgium). After overnight incubation and washing with Tris-buffered saline, Alexa Fluor 594-conjugated secondary antibody was added and incubated for 0.5 h. DAPI was used as a nuclear stain. The images were acquired using a Leica TCS SP8 confocal microscope at 200× magnification or higher.

Statistical Analysis. The normality of data distribution was tested by using the Shapiro–Wilk test.[83] The *in vitro* FACS data on the macrophage uptake efficacy of Cy5.5-HA-NPs were analyzed with one-way ANOVA with Tukey's *post hoc* test. The same test was used to study the differences in the Cy7-HA-NP uptake efficacy between the aortic, splenic, and bone marrow macrophages. This comparison was done within the same mouse group, *i.e*, 6w HFD or 12w HFD. The intergroup differences were studied for each macrophage population separately with the independent samples *t* test. To study the correlation between the HA-NP uptake and CD44 expression, and HA-binding in aortic leukocyte populations, we performed Spearman's correlation test for non-normally distributed data. Furthermore, a *t* test was performed for the following parameters: the fraction of Cy5.5-HA-NP-positive area that colocalized with macrophage staining and SUV_{max} in rabbits. The % ID in mouse aortas of two atherosclerotic mouse groups and wild-type mice were compared with one-way ANOVA with Tukey's *post hoc* test. The same analysis method was used to determine the effects of weekly dosing of HA-NPs, free HA, and PBS. All the analyses were performed using IBM SPSS Statistics 23 and setting the significance level at $p < 0.05$.

ASSOCIATED CONTENT

Supporting Information

The Supporting Information is available free of charge on the ACS Publications website at DOI: 10.1021/acsnano.7b01385.

Additional figures and methods (PDF)

AUTHOR INFORMATION

Corresponding Author

*E-mail: e.kluza@amc.uva.nl. Tel: +31(0)205665296.

ORCID

Jun Tang: 0000-0002-8285-5111
Francois Fay: 0000-0001-7405-5600
Ewelina Kluza: 0000-0002-7040-0427

Author Contributions

T.J.B., M.L.S., A.A., C.P.-M., C.C., and E.K. preformed the animal experiments. E.K., W.J.M.M., and E.L. designed the experiments and supervised them. J.T., Y.Z., and F.F. contributed to the experimental setup and practical work. B.B. and J.D. performed AFM experiments. E.K. and E.K. preformed scanning electron microscopy experiments. E.D., N.vd.W., and R.H. performed or supervised dSTORM experiments. M.N. and F.K. supervised the HA-NP preparation protocol. T.R., Z.A.F., and M.P.J.d.W. were valuable advisors. The manuscript was written through contributions of all authors. All authors have given approval to the final version of the manuscript.

Notes

The authors declare no competing financial interest.

ACKNOWLEDGMENTS

This work was supported by the National Institutes of Health grants R01 EB009638 and P01 HL131478 (Z.A.F.); R01 HL125703, R01 HL118440 and P01 HL131478 (W.J.M.M.), an American Heart Association grant 16SDG31390007 (C.P.M.), and the Netherlands Organization for Scientific Research NWO Vidi (W.J.M.M.). M.L.S. is supported by the "De Drie Lichten" Foundation in The Netherlands. A.A. is supported by the European Framework Program 7 grant (FP7-Health 309820: Nano-Athero). The authors also thank the Memorial Sloan Kettering Cancer Center's Radiochemistry & Molecular Imaging Probes Core Facility, which is supported by a National Institutes of Health grant P30 CA008748, and Sensi Pharma BV for funding.

REFERENCES

(1) Laurent, T. C. Structure of Hyaluronic Acid. In *Chemistry and Molecular Biology of the Intercellular Matrix*; Balasz, E. A., Ed.; Academic Press: London, 1970; Vol. 2, pp 703–732.

(2) Toole, B. P. Hyaluronan: From Extracellular Glue to Pericellular Cue. *Nat. Rev. Cancer* **2004**, *4*, 528–539.

(3) Petrey, A. C.; de la Motte, C. A. Hyaluronan, a Crucial Regulator of Inflammation. *Front. Immunol.* **2014**, *5*, Article 10110.3389/fimmu.2014.00101.

(4) Toole, B. P. Hyaluronan-CD44 Interactions in Cancer: Paradoxes and Possibilities. *Clin. Cancer Res.* **2009**, *15*, 7462–7468.

(5) Zöller, M. CD44: Can a Cancer-Initiating Cell Profit from an Abundantly Expressed Molecule? *Nat. Rev. Cancer* **2011**, *11*, 254–267.

(6) Misra, S.; Heldin, P.; Hascall, V. C.; Karamanos, N. K.; Skandalis, S. S.; Markwald, R. R.; Ghatak, S. Hyaluronan-CD44 Interactions as Potential Targets for Cancer Therapy. *FEBS J.* **2011**, *278*, 1429–1443.

(7) McBride, W. H.; Bard, J. B. Hyaluronidase-Sensitive Halos around Adherent Cells. Their Role in Blocking Lymphocyte-Mediated Cytolysis. *J. Exp. Med.* **1979**, *149*, 507–515.

(8) Slevin, M.; Kumar, S.; Gaffney, J. Angiogenic Oligosaccharides of Hyaluronan Induce Multiple Signaling Pathways Affecting Vascular Endothelial Cell Mitogenic and Wound Healing Responses. *J. Biol. Chem.* **2002**, *277*, 41046–41059.

(9) Rooney, P.; Kumar, S.; Ponting, J.; Wang, M. The Role of Hyaluronan in Tumour Neovascularization (Review). *Int. J. Cancer* **1995**, *60*, 632–636.

(10) Stern, R.; Asari, A. A.; Sugahara, K. N. Hyaluronan Fragments: An Information-Rich System. *Eur. J. Cell Biol.* **2006**, *85*, 699–715.

(11) Oh, E. J.; Park, K.; Kim, K. S.; Kim, J.; Yang, J. A.; Kong, J. H.; Lee, M. Y.; Hoffman, A. S.; Hahn, S. K. Target Specific and Long-Acting

DOI: 10.1021/acsnano.7b01385
ACS Nano 2017, 11, 5785–5799

Delivery of Protein, Peptide, and Nucleotide Therapeutics Using Hyaluronic Acid Derivatives. *J. Controlled Release* **2010**, *141*, 2−12.
(12) Taylor, K. R.; Trowbridge, J. M.; Rudisill, J. A.; Termeer, C. C.; Simon, J. C.; Gallo, R. L. Hyaluronan Fragments Stimulate Endothelial Recognition of Injury through TLR4. *J. Biol. Chem.* **2004**, *279*, 17079−17084.
(13) Bollyky, P. L.; Lord, J. D.; Masewicz, S. A.; Evanko, S. P.; Buckner, J. H.; Wight, T. N.; Nepom, G. T. Cutting Edge: High Molecular Weight Hyaluronan Promotes the Suppressive Effects of CD4+CD25+ Regulatory T Cells. *J. Immunol.* **2007**, *179*, 744−747.
(14) Masuko, K.; Murata, M.; Yudoh, K.; Kato, T.; Nakamura, H. Anti-Inflammatory Effects of Hyaluronan in Arthritis Therapy: Not Just for Viscosity. *Int. J. Gen. Med.* **2009**, *2*, 77−81.
(15) Forrester, J. V.; Balazs, E. A. Inhibition of Phagocytosis by High Molecular Weight Hyaluronate. *Immunology* **1980**, *40*, 435−446.
(16) Tian, X.; Azpurua, J.; Hine, C.; Vaidya, A.; Myakishev-Rempel, M.; Ablaeva, J.; Mao, Z.; Nevo, E.; Gorbunova, V.; Seluanov, A. High-Molecular-Mass Hyaluronan Mediates the Cancer Resistance of the Naked Mole Rat. *Nature (London, U. K.)* **2013**, *499*, 346−349.
(17) Burdick, J. A.; Prestwich, G. D. Hyaluronic Acid Hydrogels for Biomedical Applications. *Adv. Mater. (Weinheim, Ger.)* **2011**, *23*, H41−H56.
(18) Lo, G. H.; LaValley, M.; McAlindon, T.; Felson, D. T. Intra-Articular Hyaluronic Acid in Treatment of Knee Osteoarthritis: A Meta-Analysis. *JAMA, J. Am. Med. Assoc.* **2003**, *290*, 3115−3121.
(19) Fraser, J. R.; Laurent, T. C.; Pertoft, H.; Baxter, E. Plasma Clearance, Tissue Distribution and Metabolism of Hyaluronic Acid Injected Intravenously in the Rabbit. *Biochem. J.* **1981**, *200*, 415−424.
(20) Jadin, L.; Bookbinder, L. H.; Frost, G. I. A Comprehensive Model of Hyaluronan Turnover in the Mouse. *Matrix Biol.* **2012**, *31*, 81−89.
(21) Laznicek, M.; Laznickova, A.; Cozikova, D.; Velebny, V. Preclinical Pharmacokinetics of Radiolabelled Hyaluronan. *Pharmacol. Rep.* **2012**, *64*, 428−437.
(22) Fraser, J. R.; Laurent, T. C.; Engström-Laurent, A.; Laurent, U. G. Elimination of Hyaluronic Acid from the Blood Stream in the Human. *Clin. Exp. Pharmacol. Physiol.* **1984**, *11*, 17−25.
(23) Del Pino, P.; Yang, F.; Pelaz, B.; Zhang, Q.; Kantner, K.; Hartmann, R.; Martinez De Baroja, N.; Gallego, M.; Möller, M.; Manshian, B. B.; Soenen, S. J.; Riedel, R.; Hampp, N.; Parak, W. J. Basic Physicochemical Properties of Polyethylene Glycol Coated Gold Nanoparticles That Determine Their Interaction with Cells. *Angew. Chem., Int. Ed.* **2016**, *55*, 5483−5487.
(24) Davis, M. E.; Chen, Z.; Shin, D. M. Nanoparticle Therapeutics: An Emerging Treatment Modality for Cancer. *Nat. Rev. Drug Discovery* **2008**, *7*, 771−782.
(25) Li, S. D.; Huang, L. Pharmacokinetics and Biodistribution of Nanoparticles. *Mol. Pharmaceutics* **2008**, *5*, 496−504.
(26) Oommen, O. P.; Duehrkop, C.; Nilsson, B.; Hilborn, J.; Varghese, O. P. Multifunctional Hyaluronic Acid and Chondroitin Sulfate Nanoparticles: Impact of Glycosaminoglycan Presentation on Receptor Mediated Cellular Uptake and Immune Activation. *ACS Appl. Mater. Interfaces* **2016**, *8*, 20614−20624.
(27) Lee, S.; Choi, K. Y.; Chung, H.; Ryu, J. H.; Lee, A.; Koo, H.; Youn, I. C.; Park, J. H.; Kim, I. S.; Kim, S. Y.; Chen, X.; Jeong, S. Y.; Kwon, I. C.; Kim, K.; Choi, K. Real Time, High Resolution Video Imaging of Apoptosis in Single Cells with a Polymeric Nanoprobe. *Bioconjugate Chem.* **2011**, *22*, 125−131.
(28) Yoon, H. Y.; Koo, H.; Choi, K. Y.; Lee, S. J.; Kim, K.; Kwon, I. C.; Leary, J. F.; Park, K.; Yuk, S. H.; Park, J. H.; Choi, K. Tumor-Targeting Hyaluronic Acid Nanoparticles for Photodynamic Imaging and Therapy. *Biomaterials* **2012**, *33*, 3980−3989.
(29) Thomas, R. G.; Moon, M. J.; Kim, J. H.; Lee, J. H.; Jeong, Y. Y. Effectiveness of Losartan-Loaded Hyaluronic Acid (HA) Micelles for the Reduction of Advanced Hepatic Fibrosis in C3H/HeN Mice Model. *PLoS One* **2015**, *10*, Article e014551210.1371/journal.pone.0145512.
(30) Choi, K. Y.; Yoon, H. Y.; Kim, J. H.; Bae, S. M.; Park, R. W.; Kang, Y. M.; Kim, I. S.; Kwon, I. C.; Choi, K.; Jeong, S. Y.; Kim, K.; Park, J. H. Smart Nanocarrier Based on PEGylated Hyaluronic Acid for Cancer Therapy. *ACS Nano* **2011**, *5*, 8591−8599.
(31) Lee, S. J.; Ghosh, S. C.; Han, H. D.; Stone, R. L.; Bottsford-Miller, J.; Shen, D. Y.; Auzenne, E. J.; Lopez-Araujo, A.; Lu, C.; Nishimura, M.; Pecot, C. V.; Zand, B.; Thanapprapasr, D.; Jennings, N. B.; Kang, Y.; Huang, J.; Hu, W.; Klostergaard, J.; Sood, A. K. Metronomic Activity of CD44-Targeted Hyaluronic Acid-Paclitaxel in Ovarian Carcinoma. *Clin. Cancer Res.* **2012**, *18*, 4114−4121.
(32) Bodnár, M.; Daróczi, L.; Batta, G.; Bakó, J.; Hartmann, J. F.; Borbély, J. Preparation and Characterization of Cross-Linked Hyaluronan Nanoparticles. *Colloid Polym. Sci.* **2009**, *287*, 991−1000.
(33) Lobatto, M. E.; Fuster, V.; Fayad, Z. A.; Mulder, W. J. M. Perspectives and Opportunities for Nanomedicine in the Management of Atherosclerosis. *Nat. Rev. Drug Discovery* **2011**, *10*, 835−852.
(34) Tang, J.; Lobatto, M. E.; Hassing, L.; van der Staay, S.; van Rijs, S. M.; Calcagno, C.; Braza, M. S.; Baxter, S.; Fay, F.; Sanchez-Gaytan, B. L.; Duivenvoorden, R.; Sager, H. B.; Astudillo, Y. M.; Leong, W.; Ramachandran, S.; Storm, G.; Perez-Medina, C.; Reiner, T.; Cormode, D. P.; Strijkers, G. J.; et al. Inhibiting Macrophage Proliferation Suppresses Atherosclerotic Plaque Inflammation. *Sci. Adv.* **2015**, *1*, Article e140022310.1126/sciadv.1400223.
(35) Duivenvoorden, R.; Tang, J.; Cormode, D. P.; Mieszawska, A. J.; Izquierdo-Garcia, D.; Ozcan, C.; Otten, M. J.; Zaidi, N.; Lobatto, M. E.; van Rijs, S. M.; Priem, B.; Kuan, E. L.; Martel, C.; Hewing, B.; Sager, H.; Nahrendorf, M.; Randolph, G. J.; Stroes, E. S. G.; Fuster, V.; Fisher, E. A.; et al. A Statin-Loaded Reconstituted High-Density Lipoprotein Nanoparticle Inhibits Atherosclerotic Plaque Inflammation. *Nat. Commun.* **2014**, *5*, Article 306510.1038/ncomms4065.
(36) Fredman, G.; Kamaly, N.; Spolitu, S.; Milton, J.; Ghorpade, D.; Chiasson, R.; Kuriakose, G.; Perretti, M.; Farokhzad, O.; Farokzhad, O.; Tabas, I. Targeted Nanoparticles Containing the Proresolving Peptide Ac2−26 Protect against Advanced Atherosclerosis in Hypercholesterolemic Mice. *Sci. Transl. Med.* **2015**, *7*, Article 275ra2010.1126/scitranslmed.aaa1065.
(37) Toole, B. P.; Wight, T. N.; Tammi, M. I. Hyaluronan-Cell Interactions in Cancer and Vascular Disease. *J. Biol. Chem.* **2002**, *277*, 4593−4596.
(38) Chai, S.; Chai, Q.; Danielsen, C. C.; Hjorth, P.; Nyengaard, J. R.; Ledet, T.; Yamaguchi, Y.; Rasmussen, L. M.; Wogensen, L. Over-expression of Hyaluronan in the Tunica Media Promotes the Development of Atherosclerosis. *Circ. Res.* **2005**, *96*, 583−591.
(39) Tarkin, J. M.; Dweck, M. R.; Evans, N. R.; Takx, R. A. P.; Brown, A. J.; Tawakol, A.; Fayad, Z. A.; Rudd, J. H. F. Imaging Atherosclerosis. *Circ. Res.* **2016**, *118*, 750−769.
(40) Weber, C.; Noels, H. Atherosclerosis: Current Pathogenesis and Therapeutic Options. *Nat. Med. (N. Y., NY, U. S.)* **2011**, *17*, 1410−1422.
(41) Foley, J. P.; Lam, D.; Jiang, H.; Liao, J.; Cheong, N.; McDevitt, T. M.; Zaman, A.; Wright, J. R.; Savani, R. C. Toll-like Receptor 2 (TLR2), Transforming Growth Factor-B, Hyaluronan (HA), and Receptor for HA-Mediated Motility (RHAMM) Are Required for Surfactant Protein A-Stimulated Macrophage Chemotaxis. *J. Biol. Chem.* **2012**, *287*, 37406−37419.
(42) Noble, P. W.; Lake, F. R.; Henson, P. M.; Riches, D. W. H. Hyaluronate Activation of CD44 Induces Insulin-like Growth Factor-1 Expression by a Tumor Necrosis Factor-Alpha-Dependent Mechanism in Murine Macrophages. *J. Clin. Invest.* **1993**, *91*, 2368−2377.
(43) Schledzewski, K.; Falkowski, M.; Moldenhauer, G.; Metharom, P.; Kzhyshkowska, J.; Ganss, R.; Demory, A.; Falkowska-Hansen, B.; Kurzen, H.; Ugurel, S.; Geginat, G.; Arnold, B.; Goerdt, S. Lymphatic Endothelium-Specific Hyaluronan Receptor LYVE-1 Is Expressed by Stabilin-1+, F4/80+, CD11b+ Macrophages in Malignant Tumours and Wound Healing Tissue *in Vivo* and in Bone Marrow Cultures *in Vitro*: Implications for the Assessment of Lymphangiogene. *J. Pathol.* **2006**, *209*, 67−77.
(44) Xu, X. H.; Shah, P. K.; Faure, E.; Equils, O.; Thomas, L.; Fishbein, M. C.; Luthringer, D.; Xu, X. P.; Rajavashisth, T. B.; Yano, J.; Kaul, S.; Arditi, M. Toll-like Receptor-4 Is Expressed by Macrophages in Murine and Human Lipid-Rich Atherosclerotic Plaques and Upregulated by Oxidized LDL. *Circulation* **2001**, *104*, 3103−3108.

DOI: 10.1021/acsnano.7b01385
ACS Nano 2017, 11, 5785−5799

(45) Ley, K.; Miller, Y. I.; Hedrick, C. C. Monocyte and Macrophage Dynamics during Atherogenesis. *Arterioscler., Thromb., Vasc. Biol.* **2011**, *31*, 1506−1516.
(46) Mantovani, A. Macrophage Diversity and Polarization: *In Vivo* Veritas Time to Restore Individual Rights for IL-2 and. *Blood* **2004**, *108*, 408−409.
(47) Scott, J. E.; Chen, Y.; Brass, A. Secondary and Tertiary Structures Involving Chondroitin and Chondroitin Sulphates in Solution, Investigated by Rotary Shadowing/electron Microscopy and Computer Simulation. *Eur. J. Biochem.* **1992**, *209*, 675−680.
(48) Scott, J. E. Supramolecular Organization of Extracellular-Matrix Glycosaminoglycans, Invitro and in the Tissues. *Faseb J.* **1992**, *6*, 2639−2645.
(49) Sitia, S.; Tomasoni, L.; Atzeni, F.; Ambrosio, G.; Cordiano, C.; Catapano, A.; Tramontana, S.; Perticone, F.; Naccarato, P.; Camici, P.; Picano, E.; Cortigiani, L.; Bevilacqua, M.; Milazzo, L.; Cusi, D.; Barlassina, C.; Sarzi-Puttini, P.; Turiel, M. From Endothelial Dysfunction to Atherosclerosis. *Autoimmun. Rev.* **2010**, *9*, 830−834.
(50) Van Tits, L. J. H.; Stienstra, R.; van Lent, P. L.; Netea, M. G.; Joosten, L. A. B.; Stalenhoef, A. F. H. Oxidized LDL Enhances pro-Inflammatory Responses of Alternatively Activated M2Macrophages: A Crucial Role for Krüppel-like Factor 2. *Atherosclerosis* **2011**, *214*, 345−349.
(51) Moghimi, S. M.; Hunter, A. C.; Murray, J. C. Long-Circulating and Target-Specific Nanoparticles: Theory to Practice. *Pharmacol. Rev.* **2001**, *53*, 283−318.
(52) Ahsan, F.; Rivas, I. P.; Khan, M. A.; Torres Suárez, A. I. Targeting to Macrophages: Role of Physicochemical Properties of Particulate Carriers—liposomes and Microspheres—on the Phagocytosis by Macrophages. *J. Controlled Release* **2002**, *79*, 29−40.
(53) Zheng, Z.; Katoh, S.; He, Q.; Oritani, K.; Miyake, K.; Lesley, J.; Hyman, R.; Hamik, A.; Parkhouse, R. M.; Farr, A. G.; Kincade, P. W. Monoclonal Antibodies to CD44 and Their Influence on Hyaluronan Recognition. *J. Cell Biol.* **1995**, *130*, 485−495.
(54) Lesley, J.; Schulte, R.; Hyman, R. Binding of Hyaluronic Acid to Lymphoid Cell Lines Is Inhibited by Monoclonal Antibodies against Pgp-1. *Exp. Cell Res.* **1990**, *187*, 224−233.
(55) Lesley, J.; Hyman, R. CD44 Can Be Activated to Function as an Hyaluronic Acid Receptor in Normal Murine T Cells. *Eur. J. Immunol.* **1992**, *22*, 2719−2723.
(56) Tavakoli, S.; Asmis, R. Reactive Oxygen Species and Thiol Redox Signaling in the Macrophage Biology of Atherosclerosis. *Antioxid. Redox Signaling* **2012**, *17*, 1785−1795.
(57) Tall, A. R.; Yvancharvet, L. Cholesterol, Inflammation and Innate Immunity. *Nat. Rev. Immunol.* **2015**, *15*, 104−116.
(58) Sykes, E. A.; Chen, J.; Zheng, G.; Chan, W. C. W. Investigating the Impact of Nanoparticle Size on Active and Passive Tumor Targeting Efficiency. *ACS Nano* **2014**, *8*, 5696−5706.
(59) Albanese, A.; Tang, P. S.; Chan, W. C. W. The Effect of Nanoparticle Size, Shape, and Surface Chemistry on Biological Systems. *Annu. Rev. Biomed. Eng.* **2012**, *14*, 1−16.
(60) Lobatto, M. E.; Calcagno, C.; Millon, A.; Senders, M. L.; Fay, F.; Robson, P. M.; Ramachandran, S.; Binderup, T.; Paridaans, M. P. M.; Sensarn, S.; Rogalla, S.; Gordon, R. E.; Cardoso, L.; Storm, G.; Metselaar, J. M.; Contag, C. H.; Stroes, E. S. G.; Fayad, Z. A.; Mulder, W. J. M. Atherosclerotic Plaque Targeting Mechanism of Long-Circulating Nanoparticles Established by Multimodal Imaging. *ACS Nano* **2015**, *9*, 1837−1847.
(61) Stancu, C. S.; Toma, L.; Sima, A. V. Dual Role of Lipoproteins in Endothelial Cell Dysfunction in Atherosclerosis. *Cell Tissue Res.* **2012**, *349*, 433−446.
(62) Falk, E. Pathogenesis of Atherosclerosis. *J. Am. Coll. Cardiol.* **2006**, *47*, C7−C12.
(63) von Eckardstein, A.; Rohrer, L. Transendothelial Lipoprotein Transport and Regulation of Endothelial Permeability and Integrity by Lipoproteins. *Curr. Opin. Lipidol.* **2009**, *20*, 197−205.
(64) Sanz, J.; Fayad, Z. A. Imaging of Atherosclerotic Cardiovascular Disease. *Nature (London, U. K.)* **2008**, *451*, 953−957.
(65) Hag, A. M. F.; Pedersen, S. F.; Christoffersen, C.; Binderup, T.; Jensen, M. M.; Jørgensen, J. T.; Skovgaard, D.; Ripa, R. S.; Kjaer, A. 18F-FDG PET Imaging of Murine Atherosclerosis: Association with Gene Expression of Key Molecular Markers. *PLoS One* **2012**, *7*, Article e50908e5090810.1371/journal.pone.0050908.
(66) Zhao, Y.; Kuge, Y.; Zhao, S.; Strauss, H. W.; Blankenberg, F. G.; Tamaki, N. Prolonged High-Fat Feeding Enhances Aortic 18F-FDG and 99mTc-Annexin A5 Uptake in Apolipoprotein E-Deficient and Wild-Type C57BL/6J Mice. *J. Nucl. Med.* **2008**, *49*, 1707−1714.
(67) Tawakol, A.; Singh, P.; Mojena, M.; Pimentel-Santillana, M.; Emami, H.; Macnabb, M.; Rudd, J. H. F.; Narula, J.; Enriquez, J. A.; Través, P. G.; Fernández-Velasco, M.; Bartrons, R.; Martín-Sanz, P.; Fayad, Z. A.; Tejedor, A.; Boscá, L. HIF-1α and PFKFB3Mediate a Tight Relationship Between Proinflammatory Activation and Anerobic Metabolism in Atherosclerotic Macrophages. *Arterioscler., Thromb., Vasc. Biol.* **2015**, *35*, 1463−1471.
(68) Weigel, J. A.; Raymond, R. C.; McGary, C.; Singh, A.; Weigel, P. H. A Blocking Antibody to the Hyaluronan Receptor for Endocytosis (HARE) Inhibits Hyaluronan Clearance by Perfused Liver. *J. Biol. Chem.* **2003**, *278*, 9808−9812.
(69) Sheikine, Y.; Akram, K. FDG−PET Imaging of Atherosclerosis: Do We Know What We See? *Atherosclerosis* **2010**, *211*, 371−380.
(70) Feliu, N.; Docter, D.; Heine, M.; del Pino, P.; Ashraf, S.; Kolosnjaj-Tabi, J.; Macchiarini, P.; Nielsen, P.; Alloyeau, D.; Gazeau, F.; Stauber, R. H.; Parak, W. J. *In Vivo* Degeneration and the Fate of Inorganic Nanoparticles. *Chem. Soc. Rev.* **2016**, *45*, 2440−2457.
(71) Pérez-Medina, C.; Abdel-Atti, D.; Zhang, Y.; Longo, V. A.; Irwin, C. P.; Binderup, T.; Ruiz-Cabello, J.; Fayad, Z. A.; Lewis, J. S.; Mulder, W. J. M.; Reiner, T. A Modular Labeling Strategy for *in Vivo* PET and near-Infrared Fluorescence Imaging of Nanoparticle Tumor Targeting. *J. Nucl. Med.* **2014**, *55*, 1706−1711.
(72) Pérez-Medina, C.; Binderup, T.; Lobatto, M. E.; Tang, J.; Calcagno, C.; Giesen, L.; Wessel, C. H.; Witjes, J.; Ishino, S.; Baxter, S.; Zhao, Y.; Ramachandran, S.; Eldib, M.; Sánchez-Gaytán, B. L.; Robson, P. M.; Bini, J.; Granada, J. F.; Fish, K. M.; Stroes, E. S. G.; Duivenvoorden, R.; et al. *In Vivo* PET Imaging of HDL in Multiple Atherosclerosis Models. *JACC: Cardiovascular Imaging* **2016**, *9*, 950−961.
(73) Pérez-Medina, C.; Abdel-Atti, D.; Tang, J.; Zhao, Y.; Fayad, Z. A.; Lewis, J. S.; Mulder, W. J.; Reiner, T. Nanoreporter PET Predicts the Efficacy of Anti-Cancer Nanotherapy. *Nat. Commun.* [Online] **2016**, *7*, Article 1183810.1038/ncomms11838.
(74) El-Dakdouki, M. H.; El-Boubbou, K.; Kamat, M.; Huang, R.; Abela, G. S.; Kiupel, M.; Zhu, D. C.; Huang, X. CD44 Targeting Magnetic Glyconanoparticles for Atherosclerotic Plaque Imaging. *Pharm. Res.* **2014**, *31*, 1426−1437.
(75) Kamat, M.; El-Boubbou, K.; Zhu, D. C.; Lansdell, T.; Lu, X.; Li, W.; Huang, X. Hyaluronic Acid Immobilized Magnetic Nanoparticles for Active Targeting and Imaging of Macrophages. *Bioconjugate Chem.* **2010**, *21*, 2128−2135.
(76) Lee, G. Y.; Kim, J.-H.; Choi, K. Y.; Yoon, H. Y.; Kim, K.; Kwon, I. C.; Choi, K.; Lee, B.-H.; Park, J. H.; Kim, I.-S. Hyaluronic Acid Nanoparticles for Active Targeting Atherosclerosis. *Biomaterials* **2015**, *53*, 341−348.
(77) Juliano, R. L.; Stamp, D. The Effect of Particle Size and Charge on the Clearance Rates of Liposomes and Liposome Encapsulated Drugs. *Biochem. Biophys. Res. Commun.* **1975**, *63*, 651−658.
(78) Moore, K. J.; Tabas, I. Macrophages in the Pathogenesis of Atherosclerosis. *Cell* **2011**, *145*, 341−355.
(79) Gaffney, J.; Matou-Nasri, S.; Grau-Olivares, M.; Slevin, M. Therapeutic Applications of Hyaluronan. *Mol. BioSyst.* **2010**, *6*, 437−443.
(80) Thomas, R. G.; Moon, M.; Lee, S.; Jeong, Y. Y. Paclitaxel Loaded Hyaluronic Acid Nanoparticles for Targeted Cancer Therapy: *In Vitro* and *in Vivo* Analysis. *Int. J. Biol. Macromol.* **2014**, *72*, 510−518.
(81) Reitsma, S.; Slaaf, D. W.; Vink, H.; Van Zandvoort, M. A. M. J.; Oude Egbrink, M. G. A. The Endothelial Glycocalyx: Composition, Functions, and Visualization. *Pfluegers Arch.* **2007**, *454*, 345−359.

DOI: 10.1021/acsnano.7b01385
ACS Nano 2017, 11, 5785−5799

(82) Schindelin, J.; Arganda-Carreras, I.; Frise, E.; Kaynig, V.; Longair, M.; Pietzsch, T.; Preibisch, S.; Rueden, C.; Saalfeld, S.; Schmid, B.; Tinevez, J.-Y.; White, D. J.; Hartenstein, V.; Eliceiri, K.; Tomancak, P.; Cardona, A. Fiji: An Open-Source Platform for Biological-Image Analysis. *Nat. Methods* **2012**, *9*, 676−682.
(83) Shapiro, S. S.; Wilk, M. B. An Analysis of Variance Test for Normality (Complete Samples). *Biometrika* **1965**, *52*, 591−611.

DOI: 10.1021/acsnano.7b01385
ACS Nano 2017, 11, 5785−5799